Evaluation of GPM IMERG Early, Late, and Final Run in Precipitation Estimation and their Capability in Representing Extreme Rainfall Indices in Southwestern Iran

Mohammad Sadegh Keikhosravi-Kiany * and Robert C. Balling Jr

Posted Date: 17 June 2024

doi: 10.20944/preprints202406.1173.v1

Keywords: Precipitation estimation; Extreme precipitation indices; Southwestern Iran; GPM IMERG

 doi:10.20944/preprints202406.1173.v1

Article

Evaluation of GPM IMERG Early, Late, and Final Run in Precipitation Estimation and their Capability in Representing Extreme Rainfall Indices in Southwestern Iran

Mohammad Sadegh Keikhosravi-Kiany [1]* and Robert C. Balling Jr [2]

[1] Faculty of Geographical Sciences and Planning, University of Isfahan, Isfahan, Iran; ms.keikhosravikiany@geo.ui.ac.ir
[2] School of Geographical Sciences and Urban Planning, Arizona State University, Tempe, AZ, USA; robert.balling@asu.edu
* Correspondence: ms.keikhosravikiany@geo.ui.ac.ir; Tel.: (+989136902852)

Abstract: The growing concerns about floods have highlighted the need for accurate and detailed precipitation data as extreme precipitation occurrences can lead to catastrophic floods, resulting in significant economic losses and casualties. Integrated Multi-satellitE Retrievals for the Global Precipitation Measurement (GPM-IMERG) is a commonly used high-resolution gridded precipitation dataset and is recognized as trustworthy alternative sources of precipitation data. The aim of this study is to comprehensively evaluate the performance of GPM IMERG Early (IMERG-E), Late (IMERG-L), and Run Final (IMERG-F) in precipitation estimation and their capability in detecting extreme rainfall indices over southwestern Iran during 2001-2020. The Asfezari gridded precipitation data which are developed using a dense of ground-based observation were utilized as the reference dataset. The findings indicate that the IMERG-F performs reasonably well in capturing many extreme precipitation events (defined by various indices). All the three products showed a better performance in capturing fixed and non-threshold precipitation indices across the study region. The findings also revealed that both IMERG-E and IMERG-L have problems in rainfall estimation over elevated areas showing values of overestimations. Examining the effect of land cover type on the accuracy of the precipitation products suggest that both IMERG-E and IMERG-L show large and highly unrealistic overestimations over inland water bodies and permanent wetlands. The results of the current study highlight the potential of IMERG-F as a valuable source of data for precipitation monitoring in the region.

Keywords: Precipitation estimation; Extreme precipitation indices; Southwestern Iran; GPM IMERG

1. Introduction

Precipitation is a key part in the hydrological cycle and can lead to various natural catastrophes such as floods and droughts when it occurs in excess or deficit. As a result, monitoring precipitation is critical for understanding its impact on society and for disaster planning and mitigation [1,2]. Climate change has been impacting precipitation regimes, leading to changes in the frequency, duration, and/or intensity of precipitation events [3–7]. Rising planetary temperatures increase the atmosphere's capacity to hold water (≈7% per 1°C), which can result in greater precipitation intensity [8]. This, in turn, can lead to an increase in extreme hydrologic events, such as heavy rainfall and subsequent floods [9]. Extreme precipitation events are strongly correlated with hydro-meteorological disasters, particularly floods and landslides [10–12]. These disasters can have

 doi:10.20944/preprints202406.1173.v1

significant negative impacts on communities, leading to substantial social and economic losses [13,14]. Analyzing extreme rainfall allows scientists to better understand the underlying processes that lead to such events. Collecting high-quality precipitation data is essential for climate monitoring and for developing effective flood mitigation strategies [15,16].

Traditional precipitation measurements primarily are based on near-surface measurements collected from weather stations. While these measurements are valuable, they may not cover all areas comprehensively, leading to data sparsity in certain regions [17]. Satellite-based precipitation measurements offer a promising solution to address the issues related to data sparsity. They can provide data in regions where ground-based measurement networks are insufficient [18]. Additionally, satellite-based estimates offer continuous information with excellent spatial and temporal resolutions, allowing for continuous monitoring of rainfall events [19–21]. Among the satellite precipitation products (SPPs), IMERG is a popular satellite-based precipitation product and has been extensively assessed in many geographical territories. Following the first release of IMERG products in 2014, many researchers have analyzed the capability of IMERG precipitation products at various temporal (e.g., hourly, daily, monthly, seasonal, and annual) and spatial scales (e.g., river basin, countries, and continents) and for many applications including drought monitoring [22–24], water management [25–27], and extreme precipitation analysis [21,28–30]. Over the past years some investigations have been carried out to evaluate the capability of SPPs in detecting extreme rainfall, for instance, Zhang et al. [31] examined the accuracy of IMERG late run (IMERG-L) and IMERG final run (IMERG-F) over the North China Plain during 2000–2018 for extreme precipitation. The findings indicate that IMERG-F has a better capability at hourly, daily, and seasonal scales in comparison to the IMERG-L product.

Fang et al. [28] examined the effectiveness of IMERG and TRMM 3B42 in capturing extreme rainfall indices in China. The results revealed that these two products successfully identified underlying patterns of extreme precipitation events throughout the country. However, IMERG exhibited slightly better performance. Nepal et al. [32] examined the capability of IMERG and GSMaP-Gauge in capturing extreme precipitation indices using 279 rain gauges in Nepal over 2014-2019. The results suggest that the IMERG product was better at detecting one-day precipitation extremes, whereas GSMaP-Gauge showed a better performance in detecting duration-based and threshold extreme precipitation indices. Bakhtar et al. [33] examined the capabilities of IMERG Final Run in estimating extreme rainfall indices within Iran from 2007-2016 using daily values from a total of 281 stations. They found that the satellite product had the highest accuracy in capturing extreme precipitations in the western highlands. Conversely, the least accurate results were obtained in the Caspian Sea regions. Kiany et al. [34] assessed the effectiveness of the TRMM 3B42 dataset in replicating extreme rainfall indices. The results indicated that the TRMM 3B42 dataset can successfully capture many of the precipitation indices. Additionally, it was found to be especially accurate for both fixed and non-threshold indices.

No comprehensive study has been conducted to date to examine the accuracy of IMERG-E, IMERG-L, and IMERG-F in capturing extreme rainfall indices over southwestern Iran. Southwestern Iran is selected because Iran's biggest dams are located here with over 30 billion m^3 of reservoir storage and floods are threats in this region during the rainy seasons. This investigation can be used as an important case study for the application of IMERG products in capturing extreme precipitation indices and could be possibly helpful for developers of IMERG retrieval algorithms.

2. Study Area

The study region in southwestern Iran comprises four major rivers including the Karkheh, Karun, Jarahi, and Helleh. The terrain in this region is highly complex, with elevation ranging from sea level at along the Persian Gulf to >4000 m in the highland zones, particularly the Zagros Mountains (Figure 1). These four river basins contain several of Iran's biggest dams, which supply water to >4 million people [35]. Moreover, the Khuzestan Province in southwestern Iran is known for its high agricultural productivity. The temporal pattern of precipitation in the study region is unevenly distributed throughout the year. The majority of rainfall occurs during the low-sun season,

 doi:10.20944/preprints202406.1173.v1

while the summer experiences dry conditions. Occasionally, some precipitation may occur in the summer due to topographic or convective mechanisms. The climate in the study region is highly diverse, ranging from very warm environments in the southern portions to much cooler settings in the elevated regions. Annual rainfall varies from below 150 mm in the lowlands in the southwestern areas to >1200 mm over the eastern mountain ranges. The spatial and seasonal variations in precipitation over the study area are influenced by the complex terrain and the westerly flow originating from the Mediterranean Sea during different seasons [36].

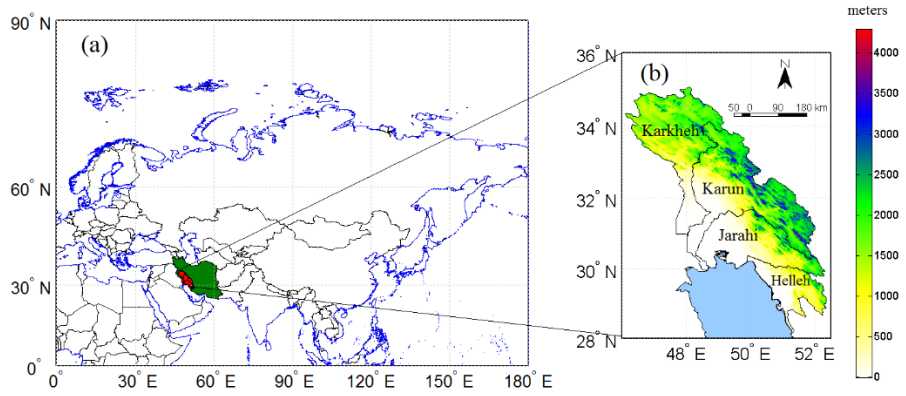

Figure 1. General location of the study region in Northern Hemisphere (a), and topography of the region (b).

3. Data

3.1. Reference Dataset

The observed precipitation dataset applied in this investigation is Asfezari gridded daily precipitation dataset. It is built on interpolations from a dense of rain gauges approximately 2200 stations in Iran and covers the country at 0.10° resolution. The dataset was developed using an ordinary Kriging method and can be classified as an interpolated gauge-based dataset [37]. This dataset has been widely used for a range of applications including calibration of satellite precipitation products, extreme precipitation analysis, and trend analysis detection **[21,38,39]**. More detailed information about the dataset is given in [40].

3.2. IMERG Products

The GPM mission is the successor to the TRMM program and involves collaboration between approximately 10 international satellites to make available global precipitation estimates. The IMERG datasets are generated from measurements made by the GPM mission, and they offer various levels of precipitation products worldwide [41].

There are three types of IMERG products:

(1) IMERG-Early: This product is accessible within four hours of when measurements are made by the satellite. Due to its short delay, it is extremely useful for real-time applications such as monitoring the effects of extreme hydrological events

(2) IMERG-Late: This product becomes available after only 14 hours since the satellite observations are made. It also has applications for real-time monitoring, though with a slightly longer delay than IMERG-Early [25,42].

(3) IMERG-Final: The IMERG-Final product takes longer to be generated, generally within approximately 3.5 months [43]. It utilizes Global Precipitation Climatology Centre (GPCC) monthly data, which is expected to result in superior accuracy and dependability compared to the first two products.

3.3. Land Cover Data

 doi:10.20944/preprints202406.1173.v1

To examine the possible impact of land surface type on precipitation estimations in SPPs, we obtained Collection 61 MODIS Land Cover (MCD12Q1) data. This dataset offers global land cover classifications on a yearly basis, with a spatial resolution of 500 × 500 m; each tile of the product consists of 2,400 rows × 2,400 columns [44]. The tiles including H21V05, H22V05, and H22V06 which provided a complete coverage of the study region were copied over 2001-2022 from https://search.earthdata.nasa.gov/search.

4. Method

Continuous metrics and classification statistics are applied for the comprehensive evaluation of the SPPs across the study area. We selected three different categorical metrics to assess the accuracy of the products in detecting rain days from days with no precipitation based on a threshold of 1 mm. The first is the probability of detection (POD) which quantitatively depicts the ability of the product to detect a precipitation event during a given day. POD is calculated as POD = H / (H + M′) where H is the number of days in which the satellite and surface measurements detect an event and M′ is the number of days when the satellite fails to detect an event recorded on the ground. The values of POD range from 0 to 1, with 1 being the desired value. Secondly, the false alarm ratio is computed as FAR = F′ / (H + F′) where F′ is the number of days in which the satellite records an event not observed at ground level. The optimum value of FAR is obviously 0. Thirdly, we computed the critical success index as CSI = H / (H + M + F′) which combines the effect of false alarms and missed events; as with POD, the desired value of CSI is 1. We also applied the root mean square error (RMSE), relative bias (BIAS), and correlation coefficient (CC) as three commonly used metrics for evaluating the accuracy of satellite precipitation observations. The RMSE not only indicates the average error between satellite and ground precipitation, but also measures the dispersion of both. The optimal value for RMSE is 0. The BIAS is not affected by the magnitude of the precipitation value and can measure the error when comparing different levels of precipitation. The optimal value for BIAS is also 0. CC measures linear correlation between two sets of data and the optimal value for CC is +1. Si denotes satellite precipitation estimation and Oi represents ground-based precipitation. The calculation formulas for each metric are shown in Table 1.

For the evaluation of IMERG data in capturing extreme precipitation indices, 11 frequently used extreme precipitation indices were selected. These indices are grouped by grid-related thresholds, fixed thresholds, and non-threshold categories based on their calculation methods [45]. The category based on fixed thresholds uses a constant threshold for all pixels (e.g., number of days with a rainfall total ≥ 10 mm), while the category based on grid-related thresholds is determined by different thresholds for each pixel based on spatial variations in annual rainfall throughout the study area. The category based on non-threshold indices (Rx1day, SDII, and PRCPTOT) are not based on specific thresholds for individual or all pixels (details are provided in Table 2).

Table 1. Applied metrics for the assessment of satellite products.

Metric	Formula	Unit
Probability of Detection (POD)	$POD = \frac{H}{H + M'}$	-
False Alarm Ratio	$FAR = \frac{F}{H + F'}$	-
Critical Success Index	$CSI = \frac{H}{H + M + F'}$	-

 doi:10.20944/preprints202406.1173.v1

Pearson Linear Correlation Coefficient	$r = \frac{\sum_{i=1}^{n}(O_i - \bar{O})(S_i - \bar{S})}{\sqrt{\sum_{i=1}^{n}(O_i - \bar{O})^2}\sqrt{\sum_{i=1}^{n}(S_i - \bar{S})^2}}$	-
Relative Bias	$RB = \frac{\sum_{i=1}^{N}(S_i - O_i)}{\sum_{i=1}^{N}(O_i)} \times 100$	percent
Root Mean Square Error	$RMSE = \sqrt{\frac{\sum_{i=1}^{n}(S_i - O_i)^2}{n}}$	mm

Table 2. Extreme rainfall indices used in this investigation.

	Index	Definition	Unit
Fixed threshold indices	R10	Total number of counts per year with precipitation ≥ 10 mm	days
	R20	Total number of counts per year with precipitation ≥ 20 mm	days
	CWD	Maximum number of consecutive wet days (CWD) annually with precipitation ≥ 1 mm	days
	CDD	Maximum number of consecutive dry days (CDD) annually with precipitation < 1 mm	days
Grid-related threshold indices	R95p	Total number of counts per year when daily precipitation > 95th percentile	days
	R99p	Total number of counts per year when daily precipitation > 99th percentile	days
	R95pTOT	Total amount of precipitation annually when daily precipitation > 95th percentile	mm
	R99pTOT	Total amount of precipitation annually when daily precipitation > 99th percentile	mm
	RX1day	Maximum one-day precipitation in a year	mm

 doi:10.20944/preprints202406.1173.v1

Non-threshold indices	SDII	Total amount of precipitation in a year divided by the total counts of days with rainfall ≥ 1 mm (Simple daily intensity index, SDII)	mm
	PRCPTOT	Total yearly precipitation when precipitation ≥1 mm	mm

5. Results and Discussion:

5.1. The Ability of the SPPs in Detecting Rainfall

The spatial distributions of the Probability of Detection (POD), False Alarm Ratio (FAR), and Critical Success Index (CSI) values are presented in Figure 2. The general results suggest that all the SPPs have a higher POD over the southwestern areas near Persian Gulf; however, the POD values are generally smaller over the northern areas indicating the products have less capability in detection of rainfall in that area. The results for FAR suggest that over the central part of the study area with moderate elevation levels, all the SPPs (particularly IMERG-F) show a good performance with FAR values generally below 0.4. The highest FAR values are seen generally over the northern regions along with some remote areas in the southwestern part of our study area. The overall results indicate the superiority of IMERG-F in terms of FAR. The Critical Success Index (CSI), which is a combination of POD and FAR, suggest that all the SPPs have a better performance over the middle areas and to the south with CSI ranging from 0.45 to 0.6.

 doi:10.20944/preprints202406.1173.v1

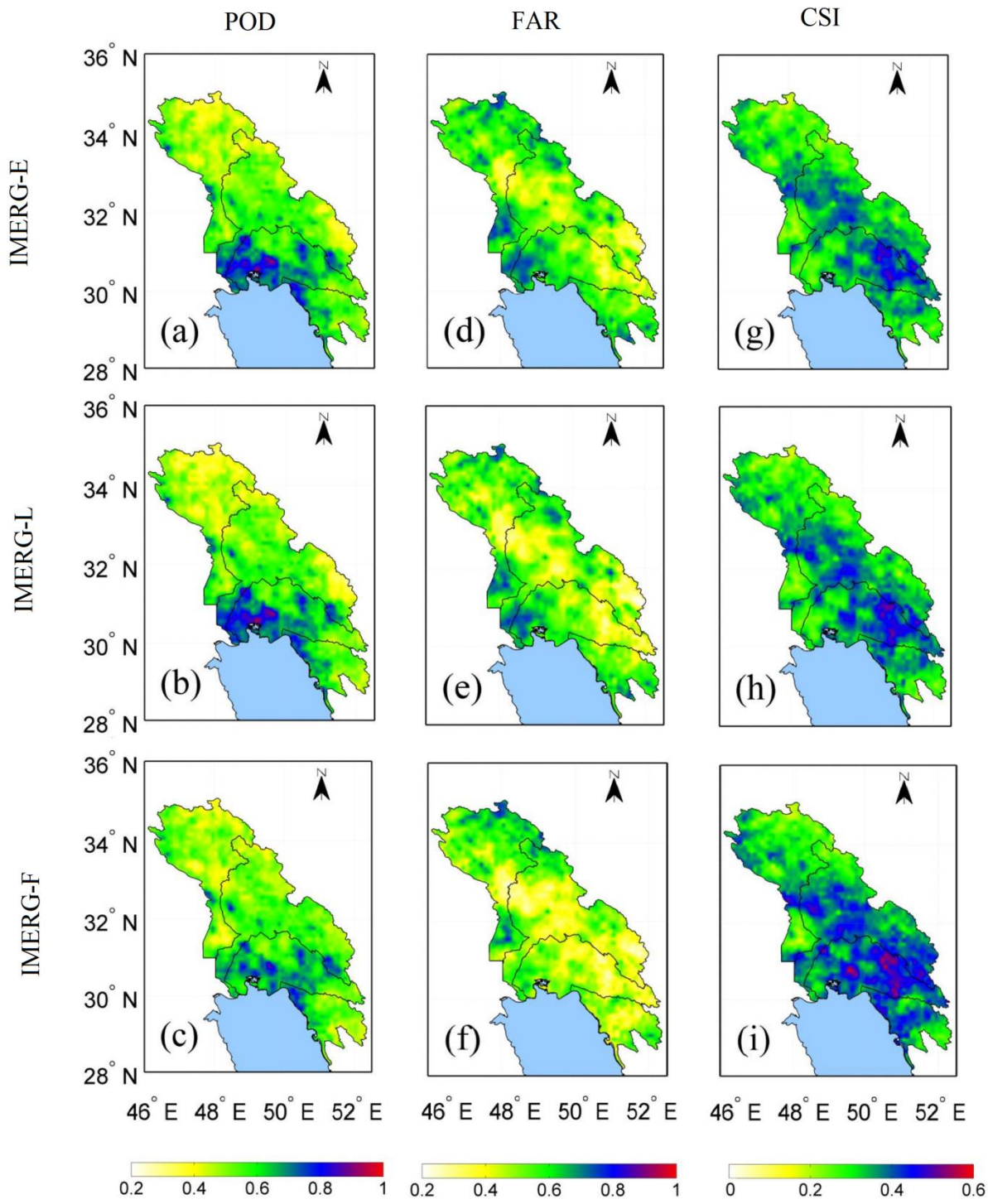

Figure 2. Spatial values of (POD), (FAR), and (CSI) in the study area.

5.2. Temporal Assessment of IMERG-E, IMERG-L, and IMERG-F

The first impression looking at Figure 3 is that all three satellite-based datasets capture the inter-monthly pattern of rainfall in southwestern Iran with the distinctive dry conditions during the summer months as the region is dominated by the subtropical high pressure belt. The IMERG-F product overestimates the Asfezari values in January while the IMERG-E and IMERG-L products over-estimate the Asfezari values in February, March, April, and May. The Asfezari data indicate meager precipitation in June, July, August, and September; however, the IMERG-E and IMERG-L products overestimate values during that time period. As precipitation increases in the fall and early winter seasons, the IMERG-E and IMERG-L products continue to substantially overestimate the

 doi:10.20944/preprints202406.1173.v1

Asfezari values particularly in October and November. The figure clearly indicates that the IMERG-F product does by far the best job reproducing the mean monthly precipitation values across the study area. Plots of seasonal precipitation totals evaluating the three satellite-based products against the Asfezari data lead to a similar conclusion. During the winter season, the IMERG-F product generates the strongest correlation, the least bias, and the least RMSE when compared to the other two products over the study period. The same is true for the spring season and IMERG-F has a particularly high correlation (0.98), essentially no bias, and a RMSE a full order of magnitude lower than the other products. In the summer season, compared to the other two, IMERG-F has the highest correlation, and bias and RMSE values an order of magnitude less than IMERG-E or IMERG-L. All three datasets do relatively well replicating precipitation totals in the fall, but once again, the IMERG-F values match remarkably well with the Asfezari data (Figure 4).

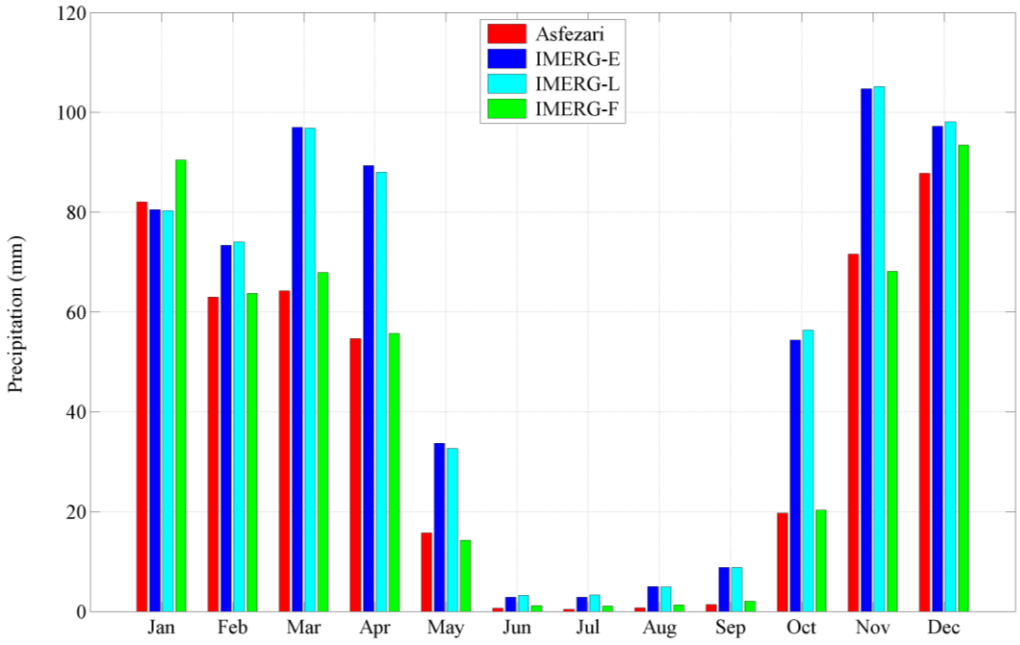

Figure 3. Monthly amount of precipitation in the study area averaged over 2001-2020 derived from Asfezari, IMERG-E, IMERG-L, and IMERG-F.

 doi:10.20944/preprints202406.1173.v1

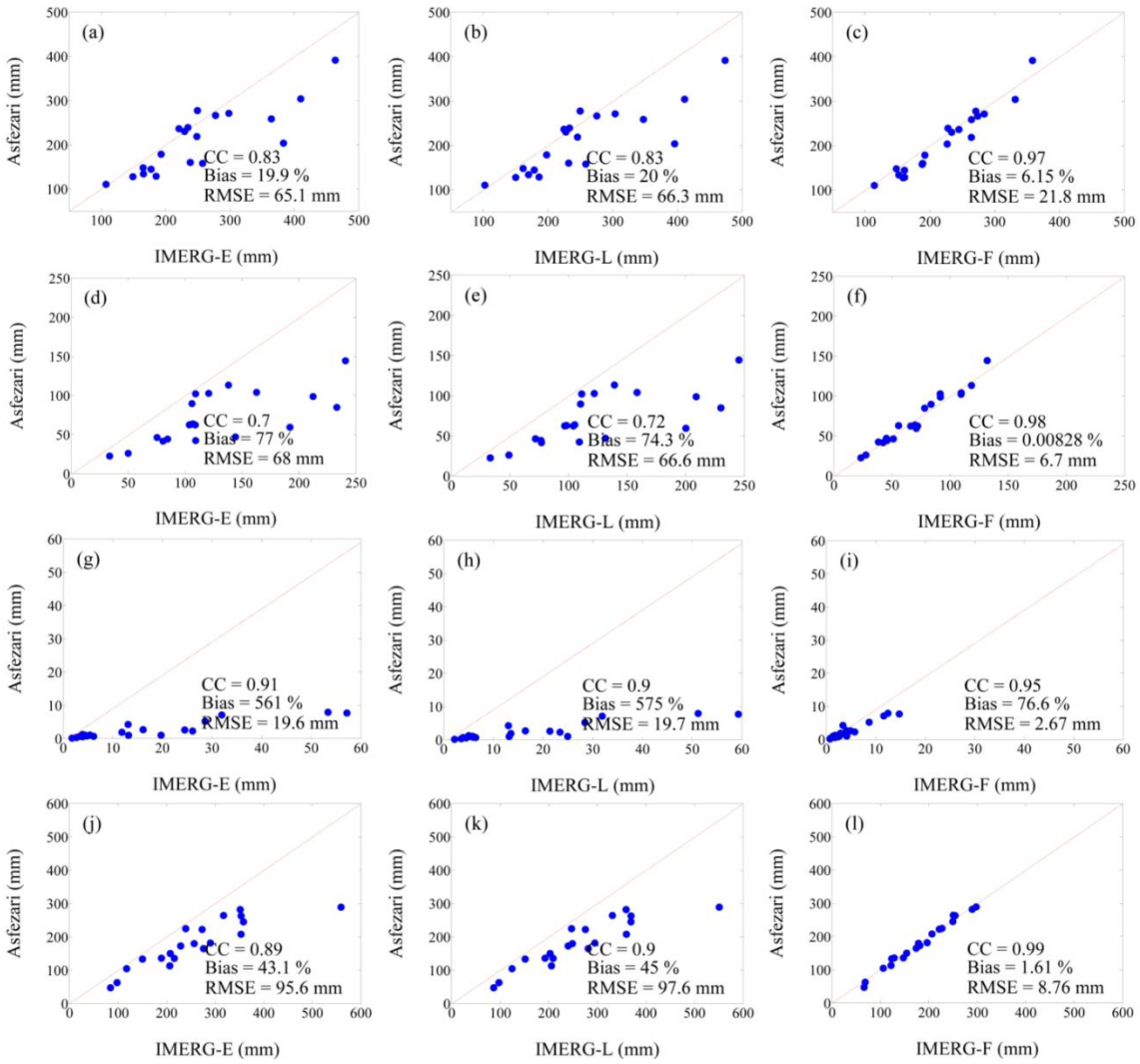

Figure 4. Scatterplots of precipitation for IMERG-E, IMERG-L, and IMERG-F compared to Asfezari for winter (a-c), spring (d-f), summer (g-i), and fall (j-l).

5.3. Spatial Assessment of IMERG-E, IMERG-L, and IMERG-F

5.3.1. . Evaluation at Seasonal Scale

Figure 5 presents seasonal precipitation totals across the study area for the gauge and satellite products. The Asfezari data reveal a winter maximum in the highland areas in the upper reaches of the Karun Basin. Precipitation values are relatively high throughout the Zagros Mountains and quite low in the coastal areas of the northern Persian Gulf. The IMERG-E and IMERG-L data underestimate the maximum values in the observational data while severely overestimating the observed low values in the coastal portions of the Jarahi Basin. The IMERG-F match the observational values relatively well in winter. The spring season spatial pattern is similar to winter, but the precipitation totals are lower overall. The IMERG-E and IMERG-L data overestimate the values in the upper reaches of the Jarahi Basin, and both produce a strange local maximum in the lower reaches of the Karkheh and Jarahi Basins. The IMERG-F values appear to match the Asfezari data quite well in the spring season. The same results appear in summer where the IMERG-F and Asfezari data match well spatially, but the IMERG-E and IMERG-F products continue to overestimate values throughout the Zagros Mountains and once again produce the strange local maxima in the southwestern lowlands in our focus area. These general results in spring appear again with the fall data as IMERG-E and IMERG-L overestimate values throughout the Zagros Mountains with the overestimation continuing toward

 doi:10.20944/preprints202406.1173.v1

the coastal areas along the Persian Gulf. The IMERG-F values appear to match the Asfezari data throughout most of the study area.

The patterns illustrated in Figure 6 correspond with the findings seen in Figure 5. During the winter, the prominent pattern is the unrealistic large precipitation totals in IMERG-E and IMERG-L that do not match the Asfezari measurements leading to near zero correlations. IMERG-F produces a much better fit in terms of correlation and/or RMSE, but the non-linearity of the pattern indicates that IMERG-F overestimates precipitation values. The situation improves for IMERG-E and IMERG-L in the spring season, but once again, IMERG-F produces a far superior fit to the observational data. IMERG-E and IMERG-L appear to overestimate summer rainfall totals; IMERG-F is much better in terms of bias and RMSE. The scatterplots for the fall season are quite similar to what we observed in the winter with a poor performance for IMERG-E and IMERG-L, and a much better match of IMERG-F with a bias of just 1.6%.

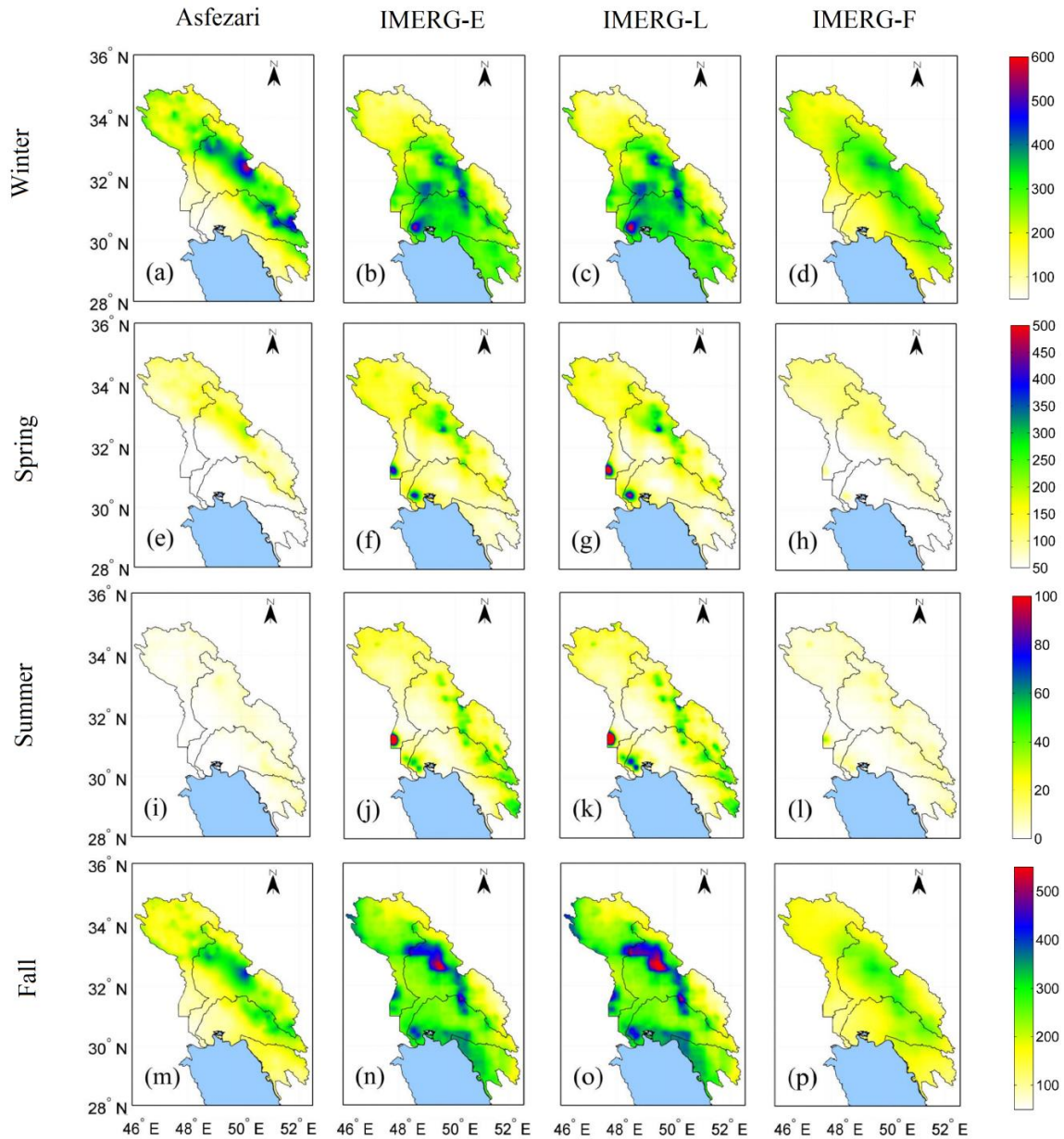

Figure 5. Seasonal values of precipitation for winter (a-d), spring (e-h), summer (i-l), and fall (m-p) derived from Asfezari, IMERG-E, IMERG-L, and IMERG-F.

Preprints.org (www.preprints.org) | NOT PEER-REVIEWED | Posted: 17 June 2024 doi:10.20944/preprints202406.1173.v1

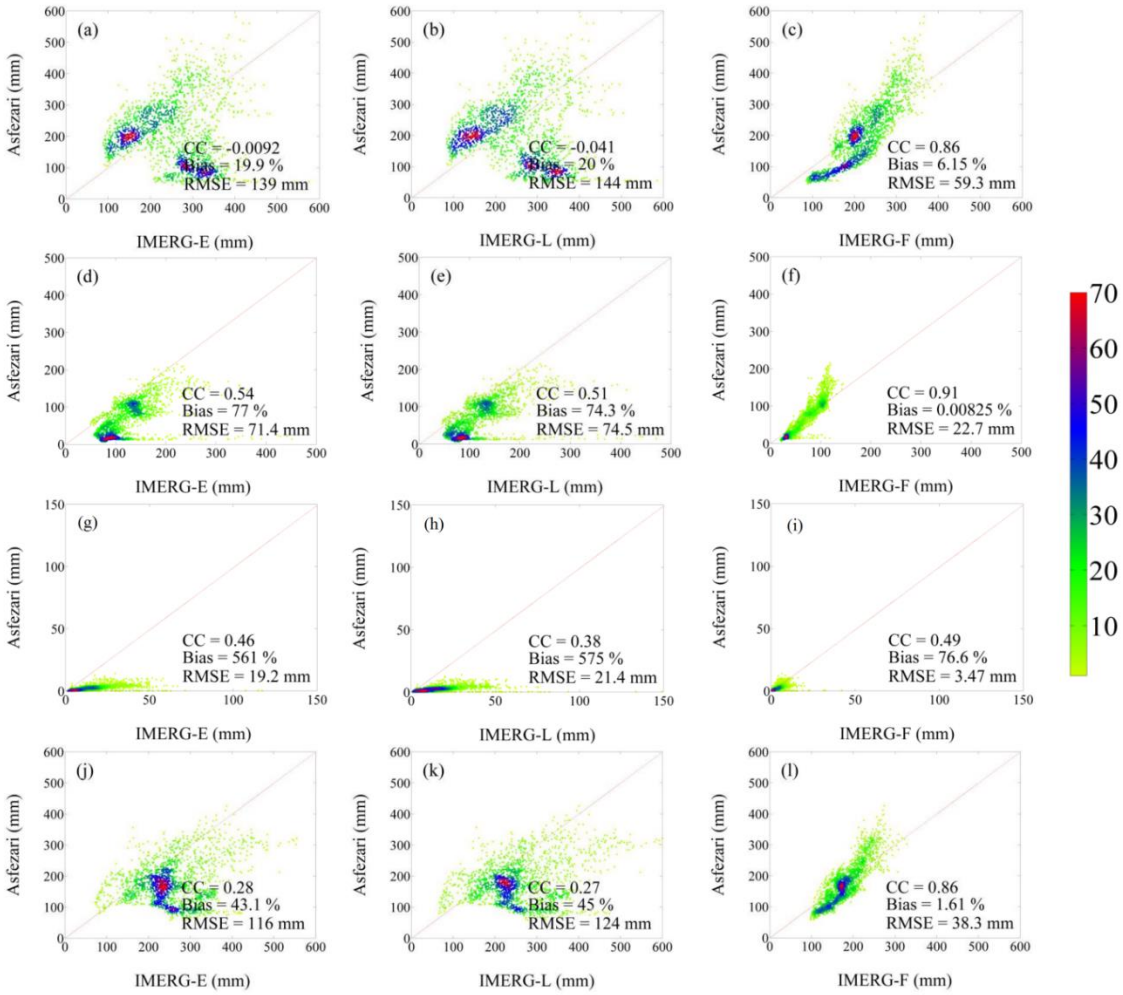

Figure 6. Density-coloured scatterplots of IMERG-E, IMERG-L, and IMERG-F against Asfezari, for winter (a–c); spring (d–f); summer (g–i), and fall (j–l) over the study region. The color represents the occurrence frequency.

5.3.2. . Evaluation at Annual Scale

Annual precipitation totals in our study area are generally high throughout the highland areas and lowest along the north coast of the Persian Gulf. IMERG-E and IMERG-L clearly overestimate the totals throughout the area, with particularly large and highly unrealistic overestimations in the coastal areas where the observational data indicate the lowest values in the region (Figure 7a, b). IMERG-F seems to slightly underestimate the annual totals in the highland areas (Figure 7c) while IMERG-E and IMERG-L overestimate the totals. The scatterplots for the annual totals clearly show that IMERG-E and IMERG-L are producing unrealistic high values where the observed totals are quite low. This mismatch is responsible to the low correlations, the high biases, and RMSE values (Figure 8a, b). The match is far better for IMERG-F in terms of all three diagnostic statistics (Figure 8c). Actually the non-linear shape of the plot is graphical evidence of the unrealistic overestimation for the IMERG-E and IMERG-L products in the region.

 doi:10.20944/preprints202406.1173.v1

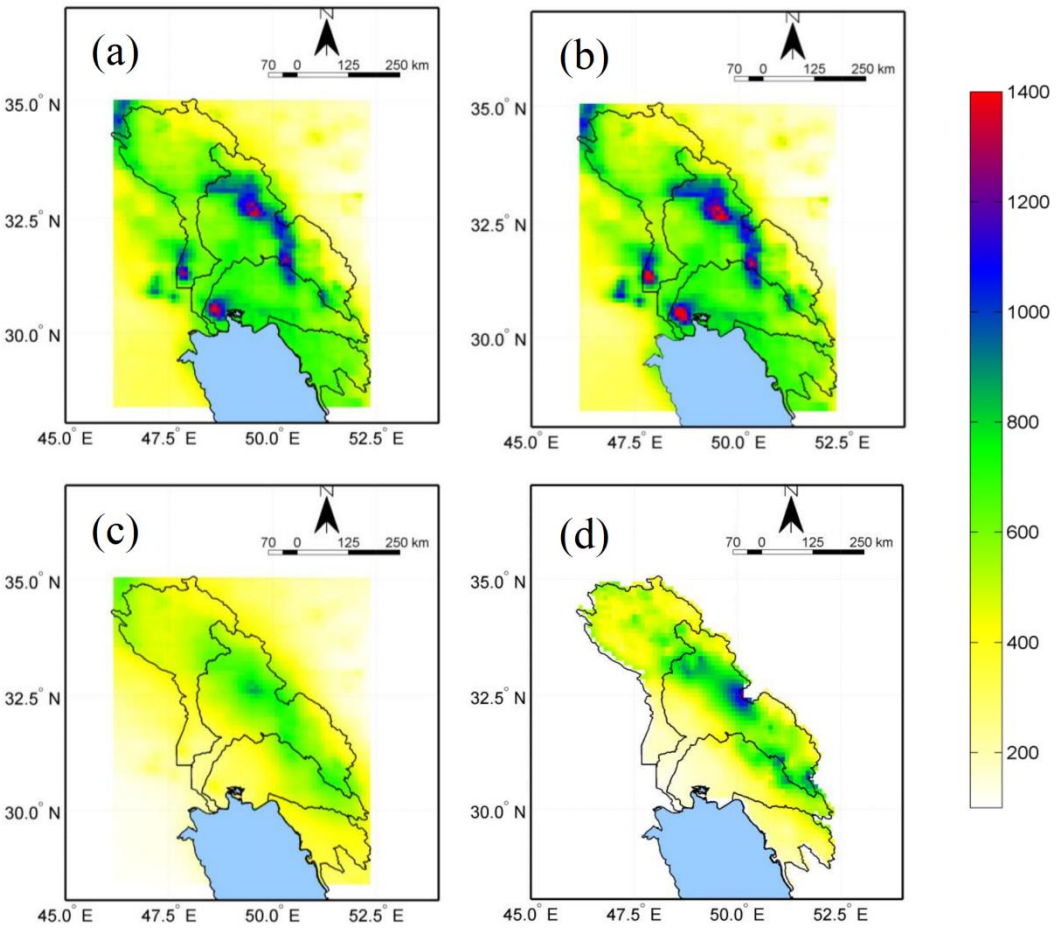

Figure 7. Annual values of precipitation derived from (a) IMERG-E, (b) IMERG-L, and (c) IMERG-F, and Asfezari (d) averaged over 2001-2020.

Preprints.org (www.preprints.org) | NOT PEER-REVIEWED | Posted: 17 June 2024 doi:10.20944/preprints202406.1173.v1

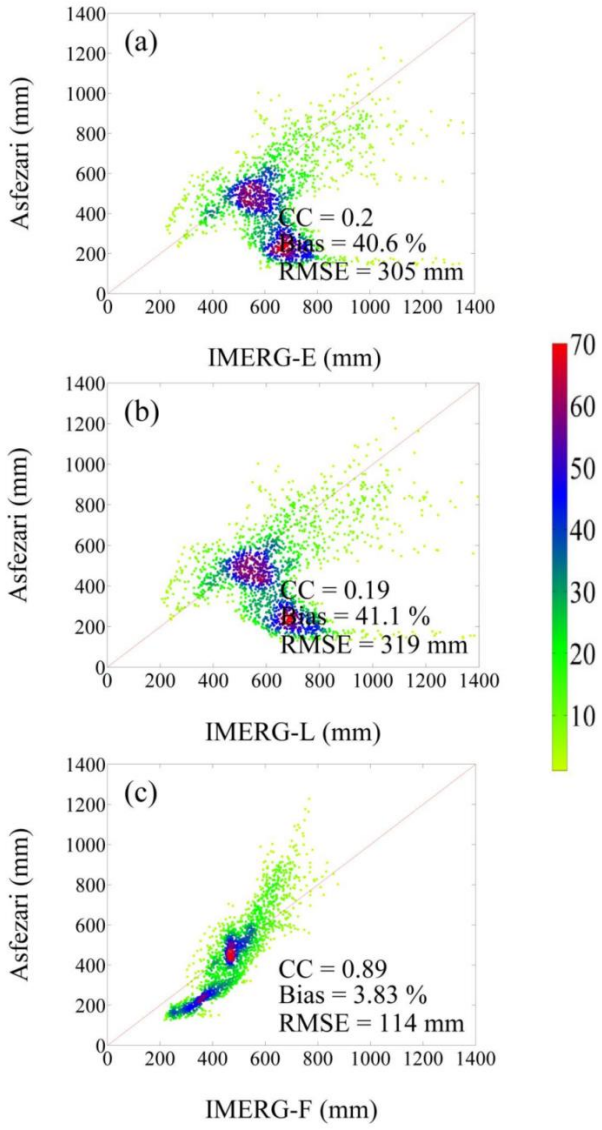

Figure 8. Annual density-coloured scatterplots of IMERG-E, IMERG-L, and IMERG-F against Asfezari over the study region. The color represents the occurrence frequency.

6. Effects of Land Cover Type on SPPs Accuracy

As discussed earlier, both IMERG-E and IMERG-L show highly unrealistic overestimations in the small areas near the coast where the observational data indicate the lowest values in the region. To examine the possible reason for these strange maximum values, the land cover features of the area were identified using MCD12Q1 product. The analysis revealed that the land cover type for these strange maxima is coded 17 and 11 which indicates water bodies and permanent wetlands, respectively (Figure 9b). It seems that the precipitation detection algorithms in both IMERG-E and IMERG-L have serious problems for detecting precipitation on internal water bodies and permanent wetlands; additionally, the rate of annual potential evaporation is substantially high in the low-lying areas in the region which complicate the correct estimation of the precipitation for the two products.

In various studies, the effect of land type on the accuracy of SPPs in identifying precipitation has also been mentioned. For example, Wolff and Fisher [46] evaluated the performance and skill of various Passive Microwave Wave (PMW) retrievals at the two ground validation sites. The results revealed that Tropical Rainfall Measuring Mission (TRMM) PMW sensors tended to overestimate precipitation rates over land and coast surfaces, while underestimating precipitation over the ocean. Keikhosravi-Kiany et al. [1] found that the light background of the Hamun region located in

 doi:10.20944/preprints202406.1173.v1

southeastern Iran has led to a mistaken identification of a relatively cloudy area, resulting in an overestimation of the rainfall amounts in that specific area by TRMM precipitation product. Therefore, understanding the source of biases in the PMW and Infrared (IR) estimates is crucial for the algorithm developers and it allows them to enhance the inter-calibration process and improve precipitation accuracy. The results clearly reveal that the utilization of GPCC data into IMERG-F estimations reduces the impact of surface type on these errors.

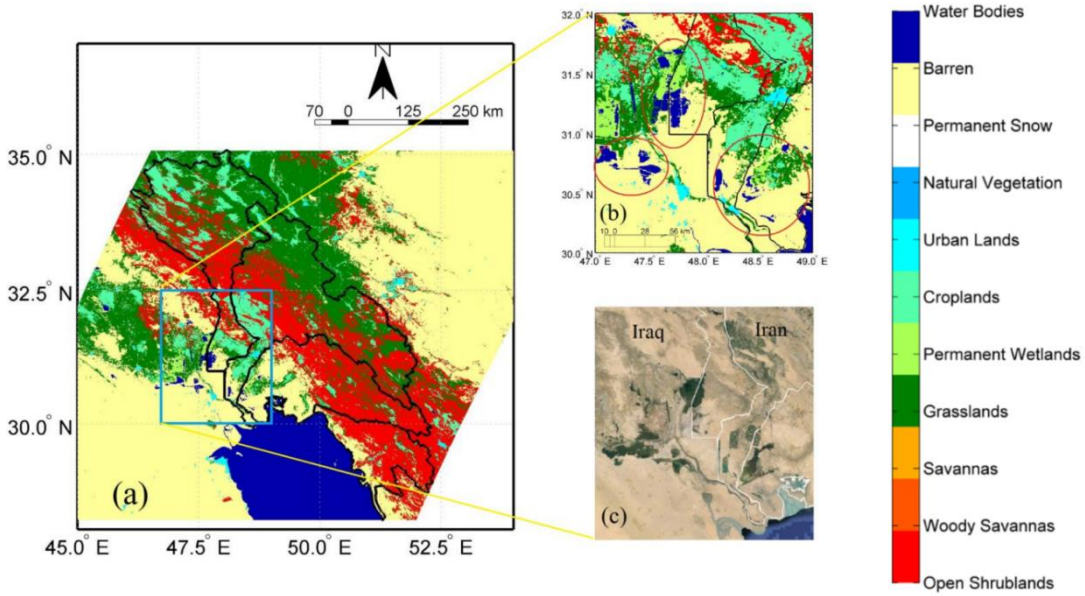

Figure 9. Land cover types of the study are derived from MCD12Q1.061 (a) along with focus on the permanent wet lands and inland water bodies (b) and Map of Google Earth image depicting earth surface features (c).

7. Effects of Elevation on SPPs Accuracy

To quantify how SPPs perform over the elevation levels, we computed the relative bias values for the annual precipitation totals for each of the 1736 pixels in the study area and compared the values to the mean elevation of each pixel. The resultant Figure 10 clearly shows that the IMERG-E and IMERG-L products produce similar patterns in the relative bias values. The comparison of the performance of SPPs shows that in total, IMERG-E and IMERG-L products show positive bias in the elevated areas, while IMERG-F depicts more values of negative bias over the highlands. As seen in section 5 of this paper, the IMERG-E and IMERG-L products severely overestimate rainfall in the lowland areas over inland water bodies and permanent wetlands which is clearly reflected in the plot (Figure 10a, b). The relative bias values for IMERG-F are generally much smaller in magnitude compared to the other two products, but there remains an increase in the positive bias values at the lowest elevations.

In line with our findings, in various studies the effects of topography on the accuracy of IMERG products have been examined. For example, Peinó et al. [47] evaluated the performance of IMERG-E, IMERG-L, and IMERG-F over the north-east (NE) of the Ibeian Peninsula in Spain. The results showed that IMERG-F underestimates precipitation over the relatively complex topography of the Pyrenees. In another study, Mahmoud et al. [48] analyzed the accuracy of IMERG products in Saudi Arabia against 275 rain gauges across the country from 2014 to 2018. The results suggest that IMERG products demonstrated a high level of detection accuracy when applied to areas of moderate elevation while their performance was notably poorer when used in coastal and mountainous regions. Navarro et al. [49] examined the accuracy of IMERG-F over Europe for 2014-2018 time period and the results revealed that despite the overall performance of the product in representing the mean precipitation, large errors appear in mountainous regions and IMERG-F underestimates values of precipitation systematically over the Scandinavian and Alps and mountains.

 doi:10.20944/preprints202406.1173.v1

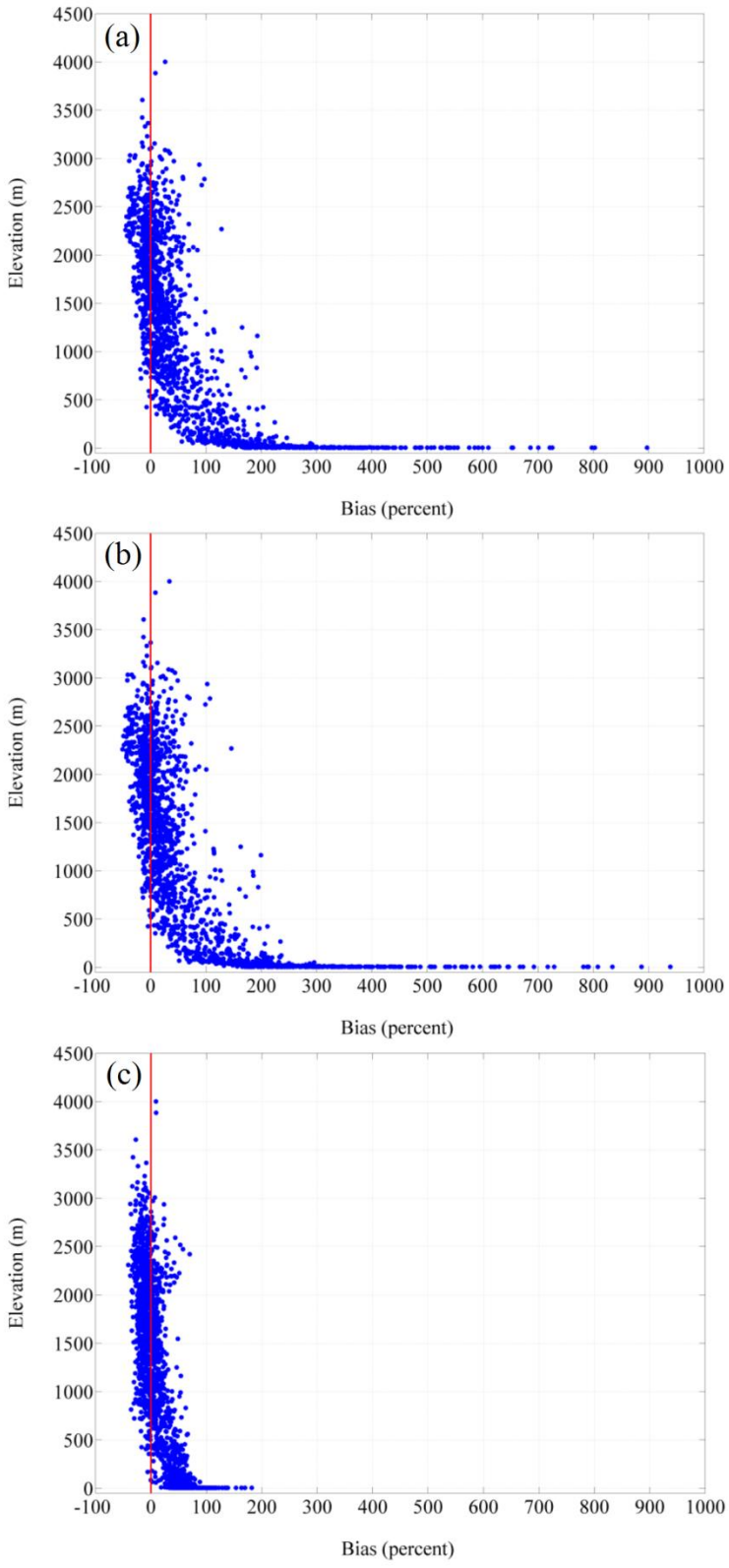

Figure 10. the bias (%) of the IMERG-E (a); IMERGE-L (b), and IMERG-F (c) against Asfezari for each of the elevation levels.

 doi:10.20944/preprints202406.1173.v1

8. Spatial Evaluation of the SPPs in Capturing Extreme Precipitation Indices

8.1. Fixed Threshold Indices

The Asfezari data clearly show that the R10 (day) values are substantially higher in the Zagros Mountains when compared to the lowlands of the study area (Figure 11a); values are particularly high in the upper reaches of the Karun basin. While the three IMERG products capture the essence of this spatial pattern, IMERG-E and IMERG-L data markedly overestimate the R10 (day) values in the lowland areas. The overestimation is particularly high in the coastal areas within the Jarahi sub-basin. The IMERG-F data match well spatially with the Asfezari pattern although the maximum values of the Karun sub-basin are underestimated in the IMERG-F data. The scatterplots in Figures 12a to 12c show that the IMERG-F data have by far the best match with the observational data based on correlation coefficients, bias, and RMSE. The IMERG-F product has a correlation with the observational data three times higher than the IMERG-E and IMERG-L products, almost no bias when compared to the other two datasets, and a RMSE half the size of the other two.

Not surprisingly, the patterns for the R20 (day) index are very similar to what was found for R10 (day) (Figures 11e-h). Again, the IMERG-E and IMERG-L datasets continue to badly overestimate the values in the lowland areas and particularly along the north coast of the Persian Gulf. The scatterplots (Figures 12d-f) show very low correlation coefficients for the IMERG-E and IMERG-L products (≤0.16) compared to the relatively high value for IMERG-F (0.78). The non-linear shape of the scatterplot for IMERG-F graphically illustrates the underestimation of the high R20 (day) values in the higher elevations of the Karun sub-basin.

The CWD (day) fixed threshold values are also highest in the mountainous areas and lowest in the lowlands; a strong maximum in these values appears in the northeastern highlands of the Karun sub-basin (Figures 11i-l). The various IMERG products generally reproduce this underlying pattern, but not as well as for the R10 (day) and R20 (day) values. All three IMERG products overestimate the values in the areas directly north of the Persian Gulf with the overestimation the least for the IMERG-F dataset. The scatterplots for CWD (day) (Figures 12g-i) show the best fit is with the IMERG-F product in which the correlation coefficient is twice as high as those for IMERG-E and IMERG-L, but the diagnostic statistics are not as strong as those for R10 (day) or R20 (day) indices.

The CDD (day) values are generally opposite of the other three fixed threshold indices with highest values along the coastal portions of the study area and lowest values in the Zagros Mountains. All three IMERG products generally capture this spatial pattern, but all three underestimate the CDD (day) values along the coast and underestimate the values in the northeastern portion of the region (Figures 11m-p). It is worth mentioning that the high frequency of precipitation estimation over some areas near the Persian Gulf in both IMERG-E and IMERG-F has led to low CDD values in this region. The scatterplots show reasonably good fits overall, but once again, the IMERG-F values have excellent correlation, bias, and RMSE values. In terms of fixed threshold indices, it is clear that IMERG-F is the best of the three products tested in our study in reproducing the patterns in the Asfezari data for the fixed threshold extreme precipitation indices. The findings of Bakhtar et al. [33] also suggest that IMERG-F shows a reasonable capability in capturing CDD over arid, semi-arid, and hyper-arid regions in Iran. Not surprisingly, the good performance of IMERG-F compared to other products is due to the incorporation of GPCC data for bias correction [50].

Preprints.org (www.preprints.org) | NOT PEER-REVIEWED | Posted: 17 June 2024 doi:10.20944/preprints202406.1173.v1

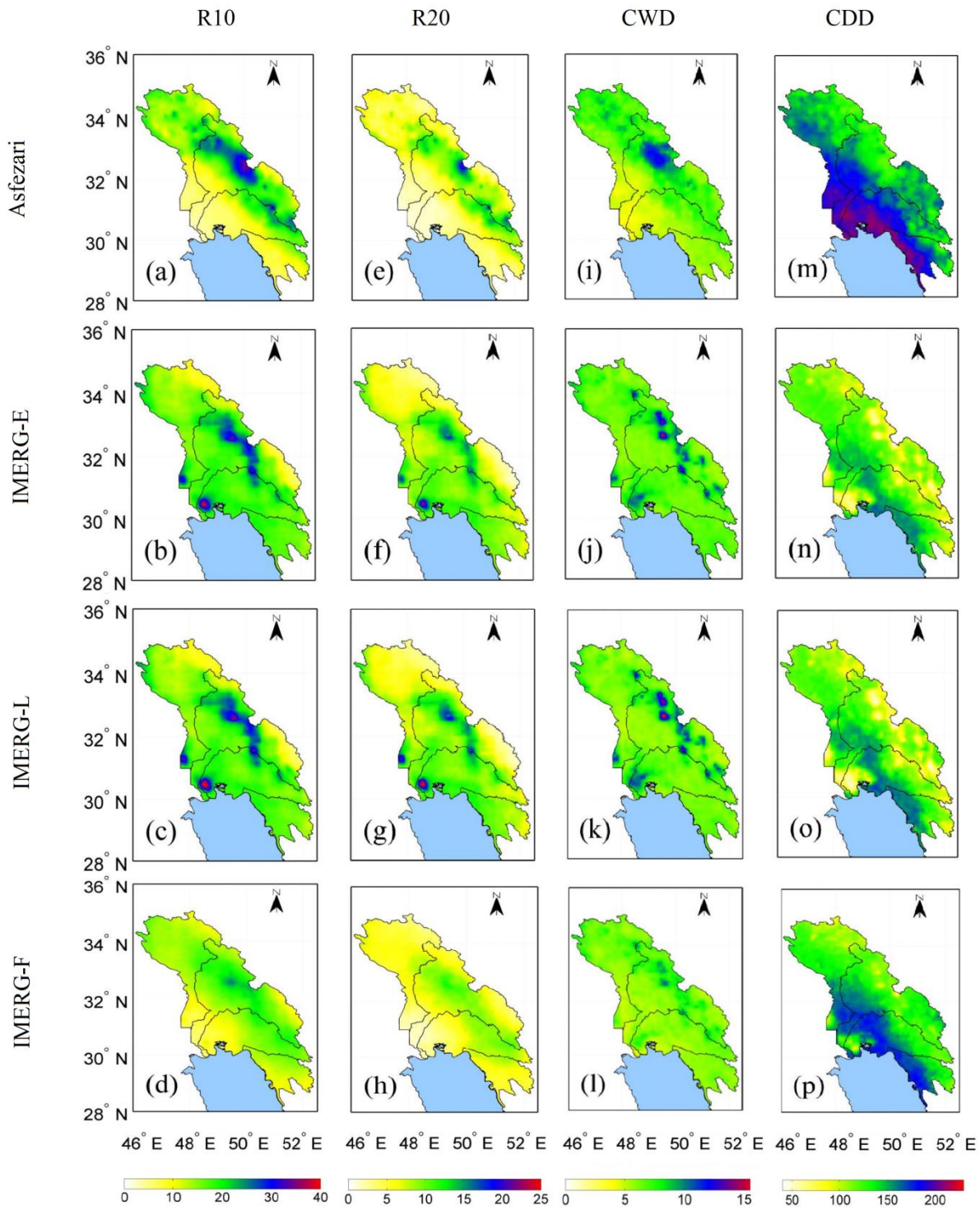

Figure 11. Long term means of fixed threshold extreme precipitation indices (R10, R20, CWD, CDD) for Asfezari, IMERG-E, IMERG-L, and IMERG-F.

 doi:10.20944/preprints202406.1173.v1

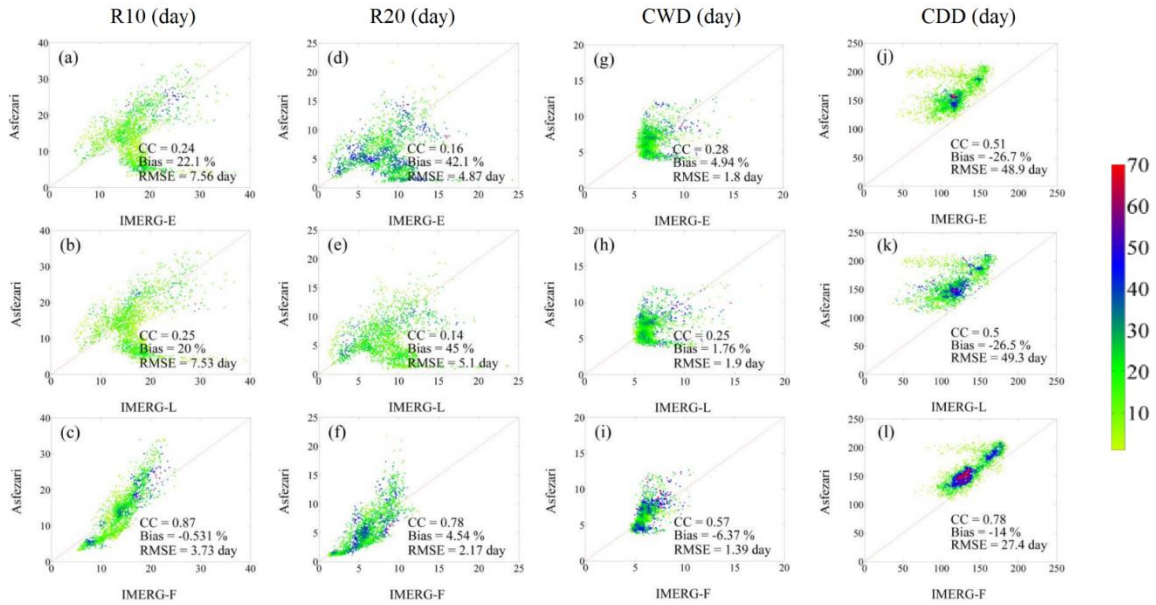

Figure 12. Density-colored scatterplots of extreme precipitation indices (R10, R20, CWD, CDD) for IMERG-E, IMERG-L, IMERG-F against Asfezari dataset. The color represents the occurrence frequency.

8.2. *Grid-Related Threshold Indices*

Many of the patterns for the grid-related thresholds are similar to those for the fixed threshold indices. The Asfezari data show that the R95 (day) spatial pattern is similar to the R10 (day) and R20 (day) indices with highest values in the central portion of the mountainous sector of the Karun sub-basin. However, all three IMERG products badly overestimate the R95 (day) values across the study area with particularly high over-estimations along the north shore to the Persian Gulf in the Jarahi sub-basin (Figure 13b-d). The scatterplots for R95 (day) (Figure 14a-c) show relatively low correlations (all <0.40) and strong positive bias values all >89%. When compared to the fixed threshold indices described earlier, the IMERG products perform relatively poorly in reproducing the observed spatial patterns for the R95p (day) index.

The situation is even worse for the R99 (day) values. All three IMERG products continue to badly overestimate values across the study area with the most egregious overestimations in the low elevation areas near the north coast of the Persian Gulf. The scatterplots (Figure 14d-f) show correlation coefficients all ≤0.17 indicating less than 3% shared variance with the spatial pattern in the observational data.

The observational data show that the R95TOT (day) values are highest in the upper areas of the Karun sub-basin and the three IMERG products capture that element of the spatial pattern (Figure 13j-l). However, the IMERG-E and IMERG-L products produce spurious and very high values in the lower portions of the Karun sub-basin while the IMERG-F values match the Asfezari pattern quite well. The IMERG-E and IMERG-L products overestimate the high values of R95TOT (day) found near the center of our study area. The scatterplots (Figure 14g-i) clearly show the superior performance of IMERG-F in replicating the observed R95TOT (day) values. The correlation for IMERG-F is 0.83 compared to 0.14 and 0.11 for the other products. And while the bias for IMERG-F is relatively high at 55.6%, the value is far less than the 114% and 128% bias values for the other two products. Not surprisingly, very similar results are found for the R99TOT (day) values. All three products overestimate these grid-related extreme precipitation values across our study area, but the bias for IMERG-F is less than half of IMERG-E or IMERG-L. Furthermore, the correlation for IMERG-F is much better than the other two and the RMSE is less than half of the values for IMERG-E or IMERG-L.

 doi:10.20944/preprints202406.1173.v1

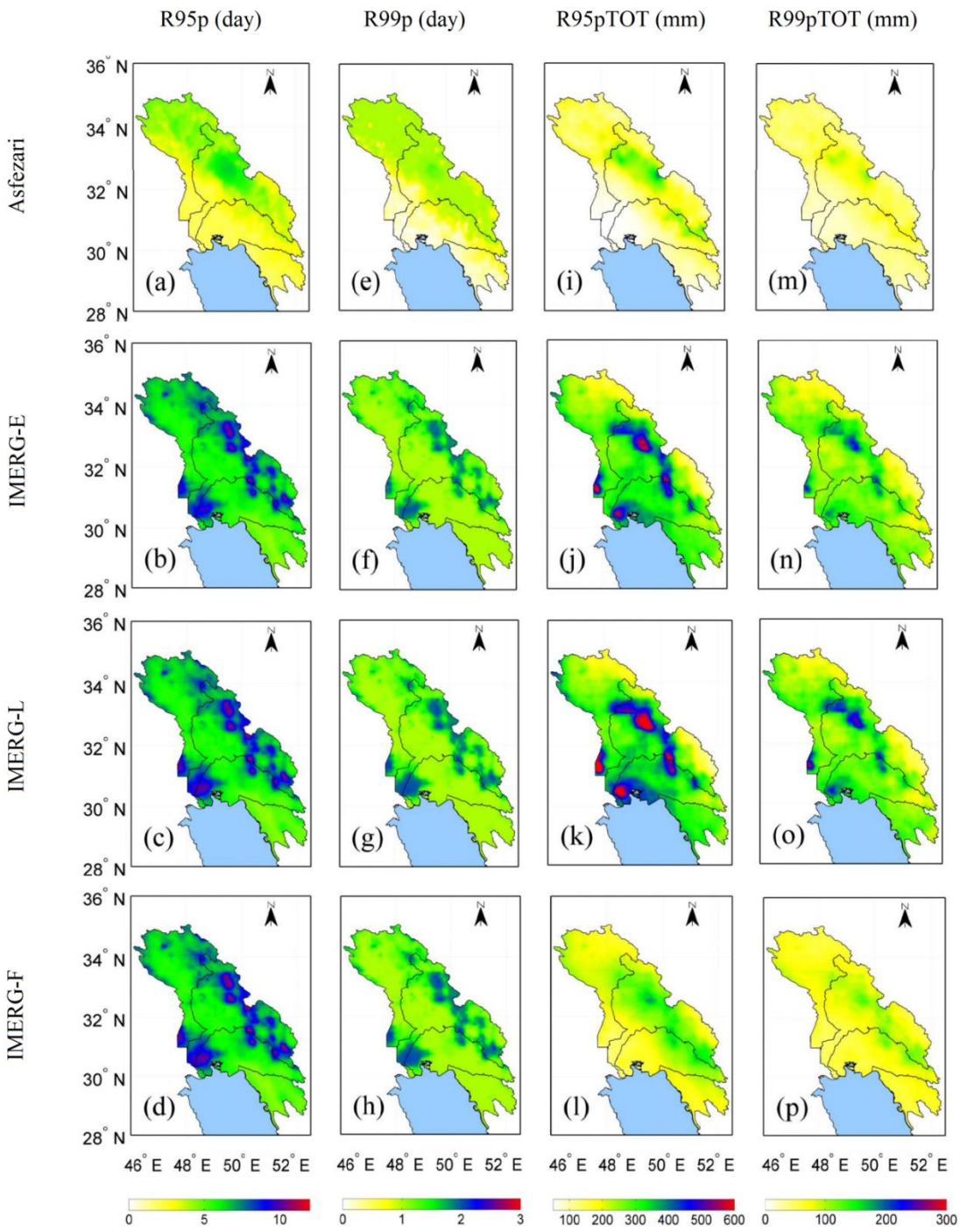

Figure 13. Long term means of grid-related extreme precipitation indices (R95p, R99p, R95pTOT and R99pTOT) for Asfezari, IMERG-E, IMERG-L, and IMERG-F.

Preprints.org (www.preprints.org) | NOT PEER-REVIEWED | Posted: 17 June 2024 doi:10.20944/preprints202406.1173.v1

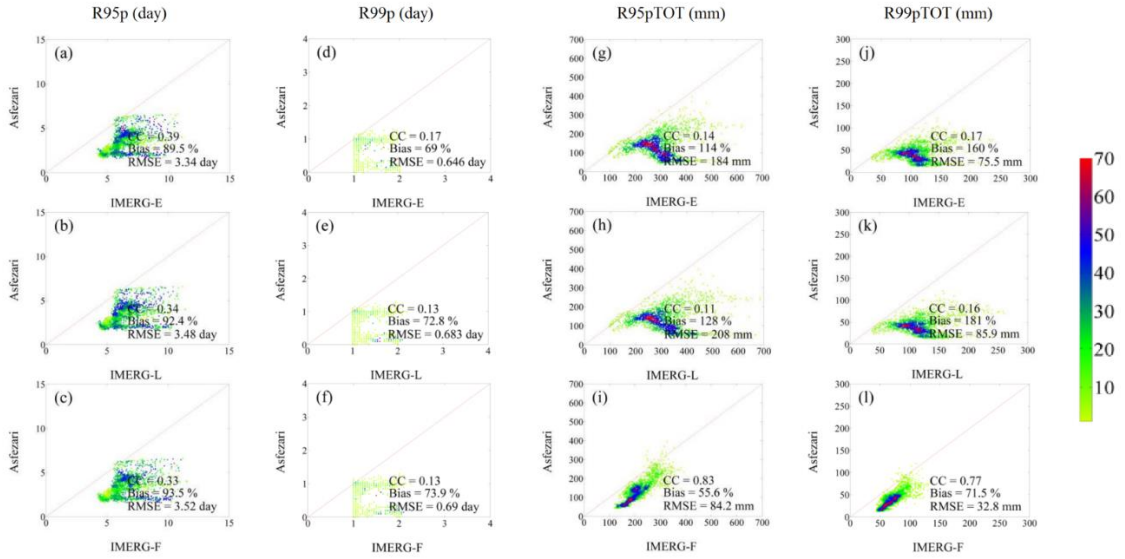

Figure 14. Density-colored scatterplots of extreme precipitation indices (R95p, R99p, R95pTOT and R99pTOT) for IMERG-E, IMERG-L, and IMERG-F against Asfezari dataset. The color represents the occurrence frequency.

8.3. Non-Threshold Indices

All the indices including Rx1day, SDII, and PRCPTOT show similar spatial patterns in terms of the observational data and the representations of the three IMERG products. The Rx1day values are relatively high in various parts of the mountainous areas of our study. IMERG-E and IMERG-L badly overestimate the values in the northern part of the Karun sub-basin and along the lowland areas on the northern coast of the Persian Gulf. The IMERG-F values are a far better match based on the maps in Figures 15a and 15d. The scatterplots (Figures 16a-c) clearly show that IMERG-F has a much higher correlation and considerably lower bias and RMSE in comparison to the other products.

The SDII patterns are similar to what we identified for the Rx1day index. The highest values for SDII are located in the mountainous areas in the southern portion of our study area. IMERG-E and IMERG-L miss this pattern all together with their maximum values along the coastal areas. Once again, visual inspection of the maps (Figures 15e-h) reveals a far better match for the IMERG-F dataset. In a similar investigation, Asku et al. [51] examined the ability of IMERG-E, IMERG-L, and IMERG-F in showing extreme indices across the Turkey, the results revealed that the IMERG-F can much better capture the Rx1day and SDII compared to IMERG-E, IMERG-L. The scatterplots (Figures 16d-f) reinforce the superiority of IMERG-F in representing the SDII index; IMERG-F has a much higher correlation and far lower bias and RMSE compared to IMERG-E and IMERG-L.

Finally, the highest values for the PRCPTOT are found throughout the Zagros Mountain portion of southwestern Iran and lowest values are in all directions away from the mountainous terrain, particularly toward to north coast of the Persian Gulf. The IMERG-E and IMERG-L products overestimate the values all across the study area, with the highest overestimations in the lowland coastal regions. As with the other two non-threshold indices, IMERG-F values appeared to match the observational data quite well (Figures 15i and l). Similarly, Bakhtar et al. [33] have shown that IMERG-F can successfully capture PRCPTOT over the Zagros Mountains and eastern Alborz regions in Iran. The scatterplots for PRCPTOT (Figures 16g-i) clearly show that the IMERG-F product is far better in replicating the Asfezari observational data for PRCPTOT given a much higher correlation and considerably lower bias and RMSE. The non-linear nature for the PRCPTOT plot suggests that the IMERG-F product tends to underestimate the highest values in the study area.

 doi:10.20944/preprints202406.1173.v1

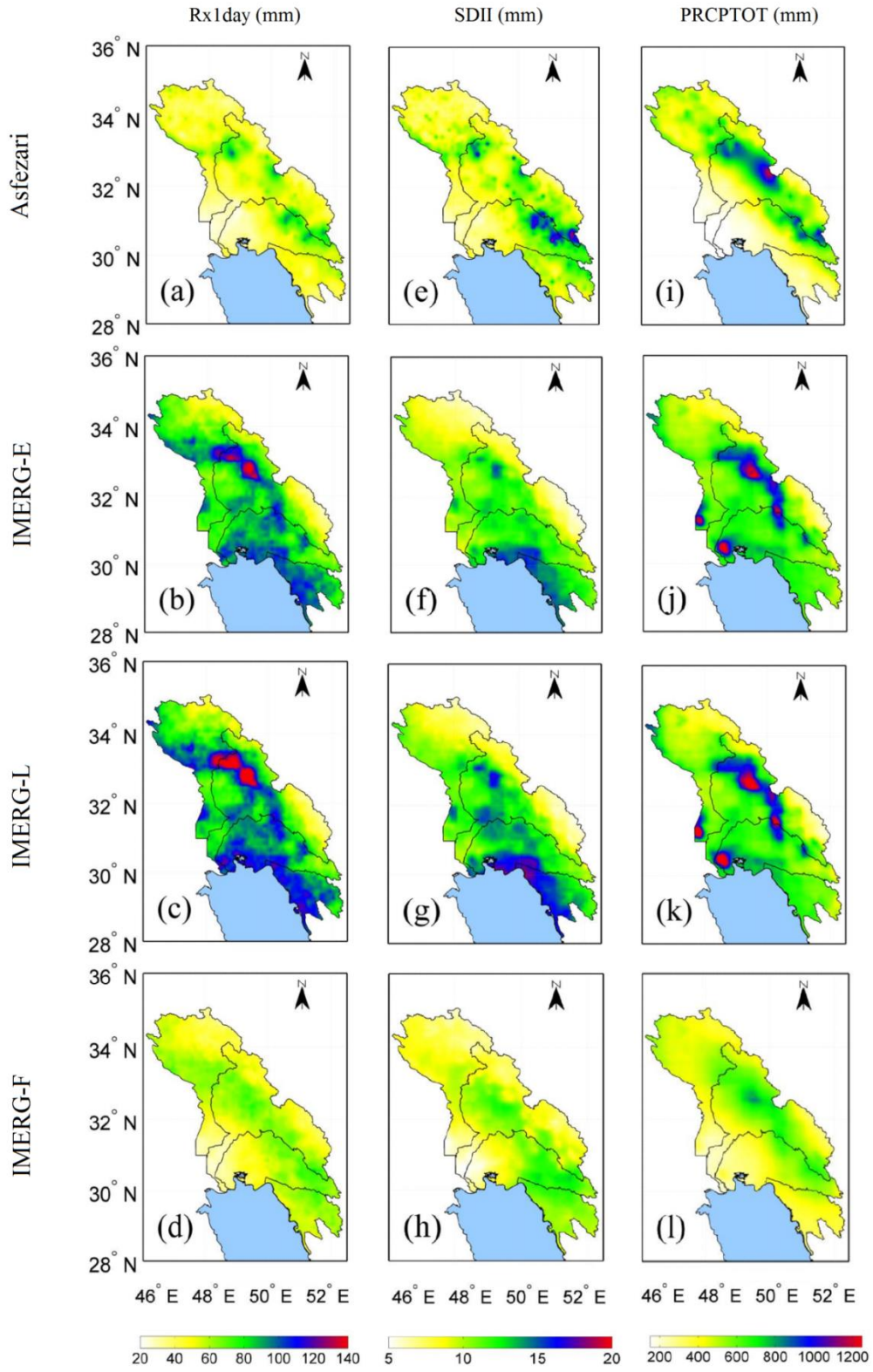

Figure 15. Long term means of non-threshold indices extreme precipitation indices (Rx1day (mm), SDII (mm), PRCPTOT (mm)) for Asfezari, IMERG-E, IMERG-L, IMERG-F.

 doi:10.20944/preprints202406.1173.v1

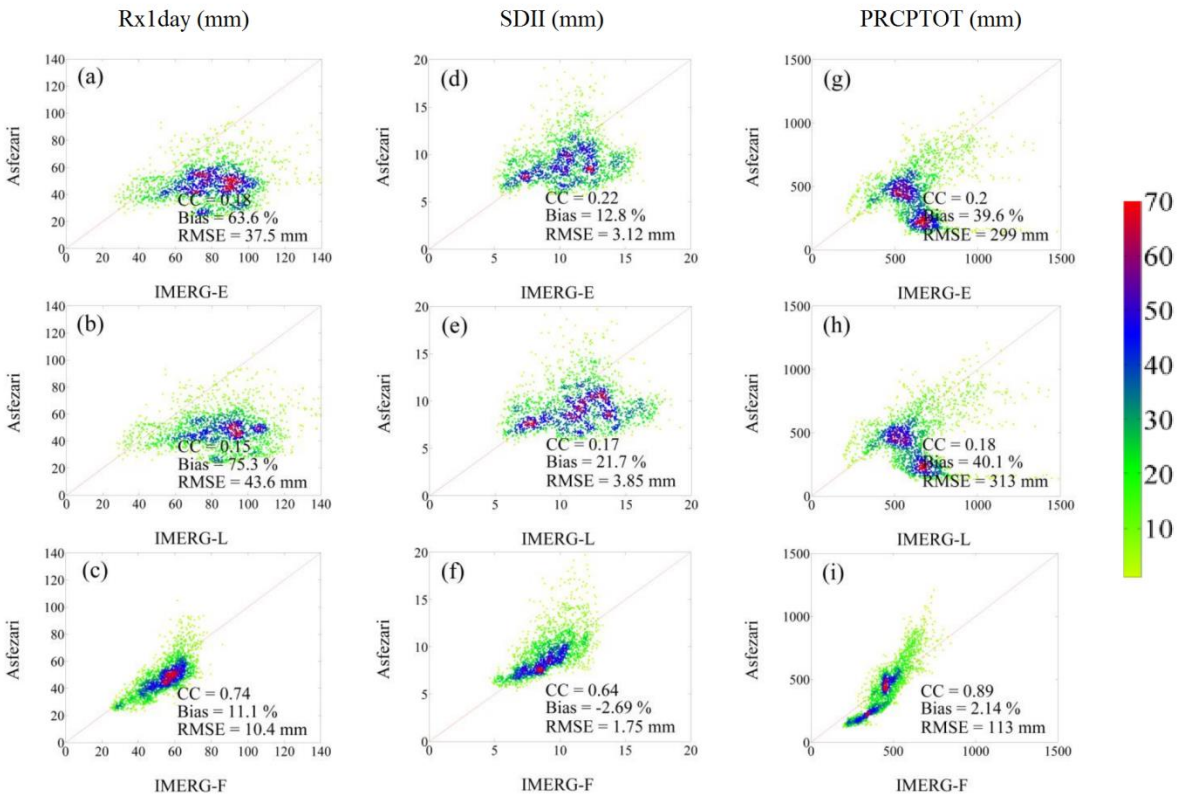

Figure 16. Density-colored scatterplots of extreme precipitation indices (Rx1day, SDII, PRCPTOT) for IMERG-E, IMERG-L, IMERG-F against Asfezari dataset. The color represents the occurrence frequency.

9. Temporal Evaluation of the SPPs in Detecting Extreme Precipitation Indices

To assess the accuracy of SPPs in representing the extreme indices temporally, we calculated the mean of each precipitation index for the study region along with "box and whisker plots" for the Asfezari, IMERG-E, IMERG-L, and IMERG-F datasets and for each index as a further graphical depiction of the distributions. The time series plot in Figure 17 indicates that all of the satellite-based products generally follow the inter-annual variations in the R10 (day) index. However, closer inspection reveals that IMERG-E and IMERG-L consistently overestimate the results from the observational Asfezari data; the overestimation is especially large in the most recent years of the study. This overestimation for the IMERG-E and IMERG-L products is seen clearly in the box and whisker plots of Figure 18. Both of these figures (17 and 18) reveal that the IMERG-F product generates values of R10 (day) that closely follow the observational data.

Not surprisingly, the same patterns are seen for the similar R20 (day) index. All three satellite-based products follow the inter-annual variations in the CWD (day) index over the study period, but the values generated from the IMERG-F product rather consistently underestimate the annual values while IMERG-E values tend to overestimate the CWD (day) values. The temporal variation figure for the CDD (day) index indicates that all three IMERG products underestimate the annual values with IMERG-E and IMERG-L underestimating the values more than IMERG-F; the result is clearly seen in the box and whisker plots.

All three satellite-based products generate inter-annual values for the R95p (day) index that generally follow the variations in the observational data; but while all three produce similar values each year, they consistently and rather badly overestimate the R95p (day) values, often by a factor of two (Figure 19 and 20). Nearly identical conclusions are reached looking at the figures for the similar R99p (day) index. The IMERG-E and IMERG-L products produce similar results for the R95pTOT index, but both consistently overestimate the observed values. IMERG-F also overestimates the

 doi:10.20944/preprints202406.1173.v1

R95pTOT values, but not as badly as the other two products. That situation is largely the same looking at the time series and box and whisker plots for the R99pTOT index.

All three non-threshold indices (RX1day, SDII, PRCPTOT) show similar patterns as we compare the observational data to the values generated by the various satellite products. IMERG-E and IMERG-L produce quite similar results, particularly for RX1day and PRCPTOT, but for all three non-threshold indices, they rather consistently overestimate the values. Inspection of the time series and box and whisker plots clearly shows that the IMERG-F product is superior in representing all three non-threshold indices (Figure 21 and 22).

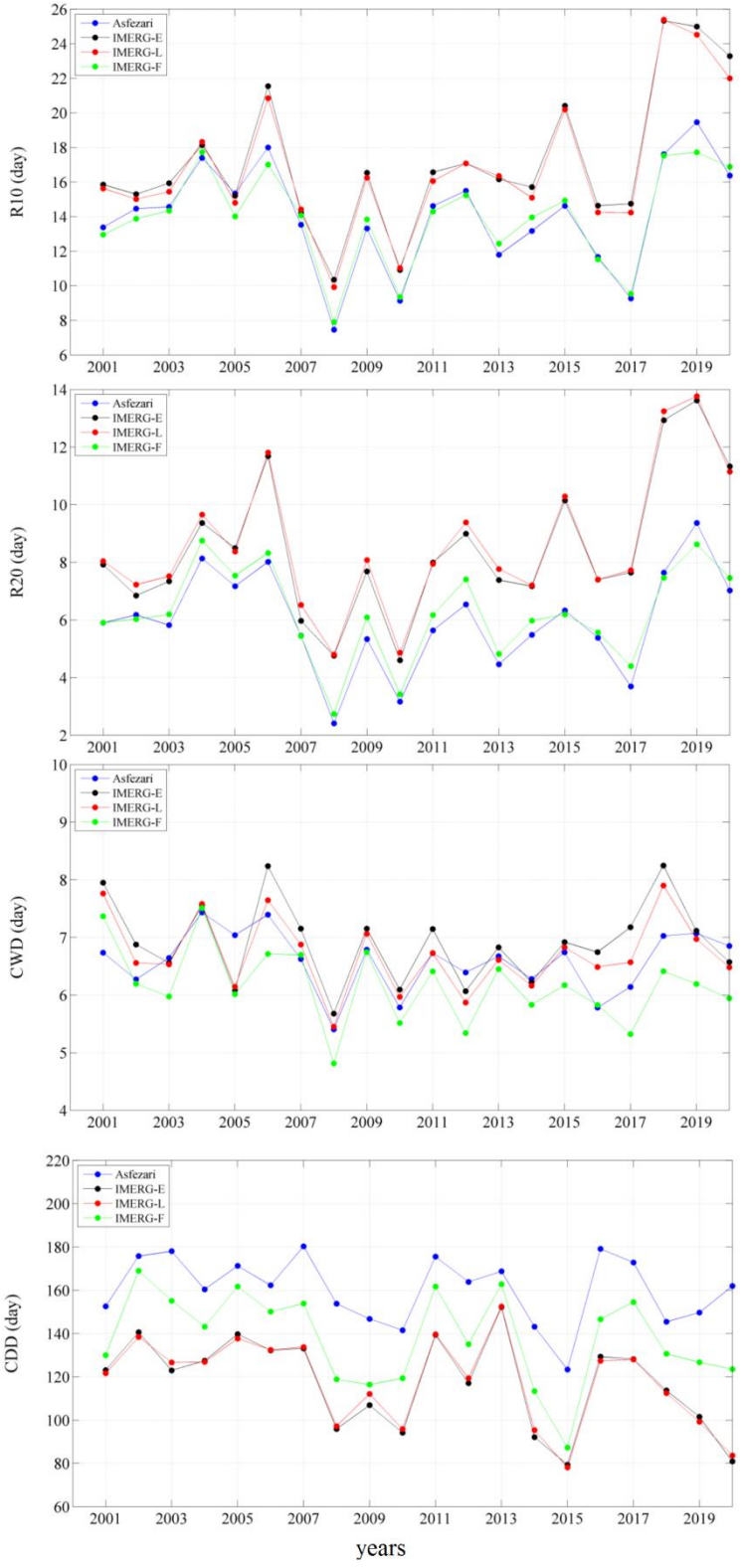

 doi:10.20944/preprints202406.1173.v1

Figure 17. temporal variation of the fixed threshold indices generated from Asfezari, IMERG-E, IMERG-L, and IMERG-F over 2001–2020.

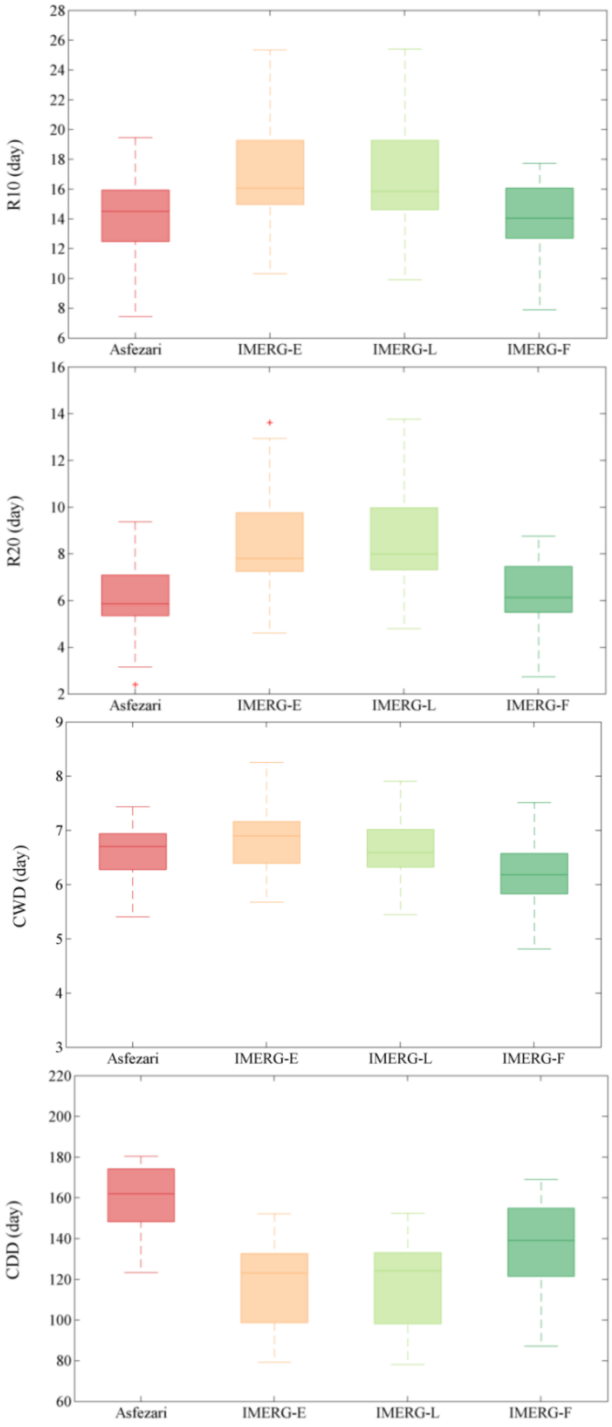

Figure 18. Relevant error box plots for Asfezari, IMERG-E, IMERG-L, and IMERG-F for fixed threshold indices. The whiskers denote the maximum and minimum values in the data. The boxes extending from Q1 to Q3 show the median (red horizontal line) while the red + symbols show outliers.

 doi:10.20944/preprints202406.1173.v1

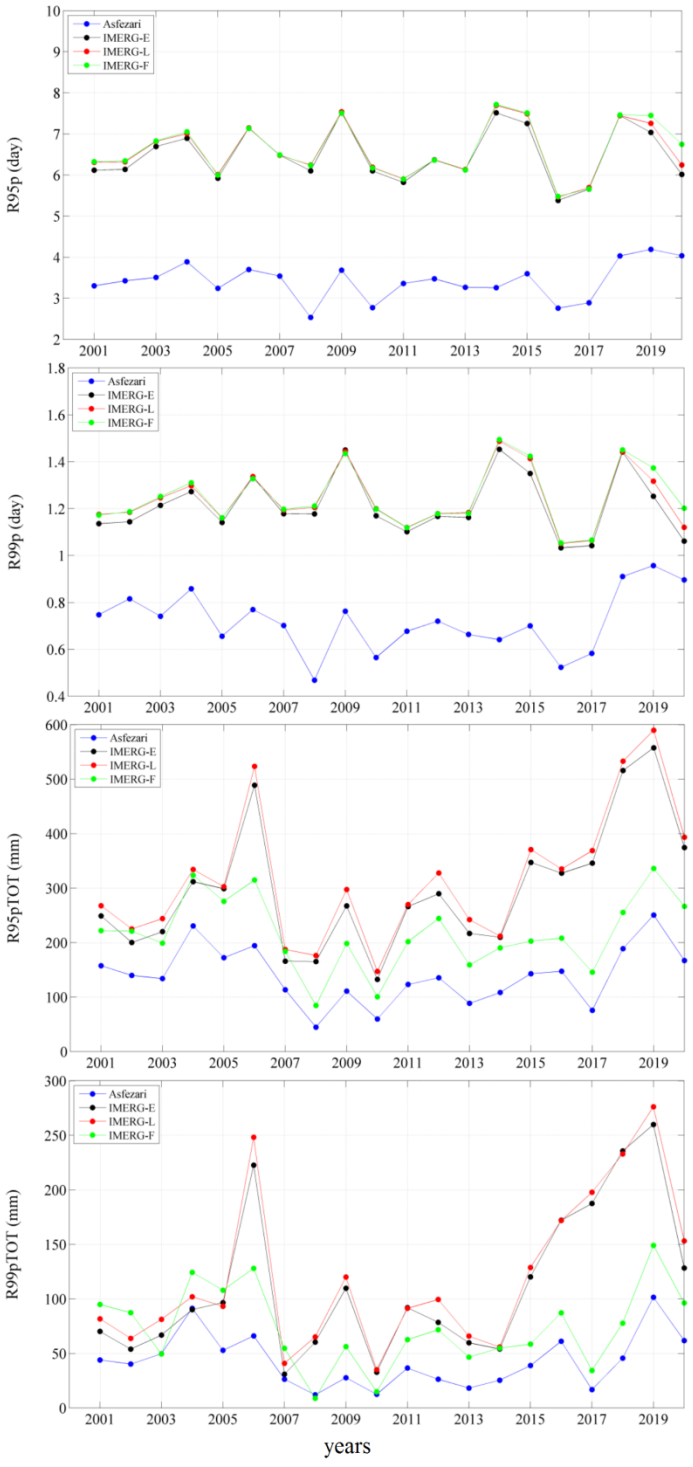

Figure 19. temporal variation of the grid-related threshold indices generated from Asfezari, IMERG-E, IMERG-L, and IMERG-F over 2001–2020.

Preprints.org (www.preprints.org) | NOT PEER-REVIEWED | Posted: 17 June 2024 doi:10.20944/preprints202406.1173.v1

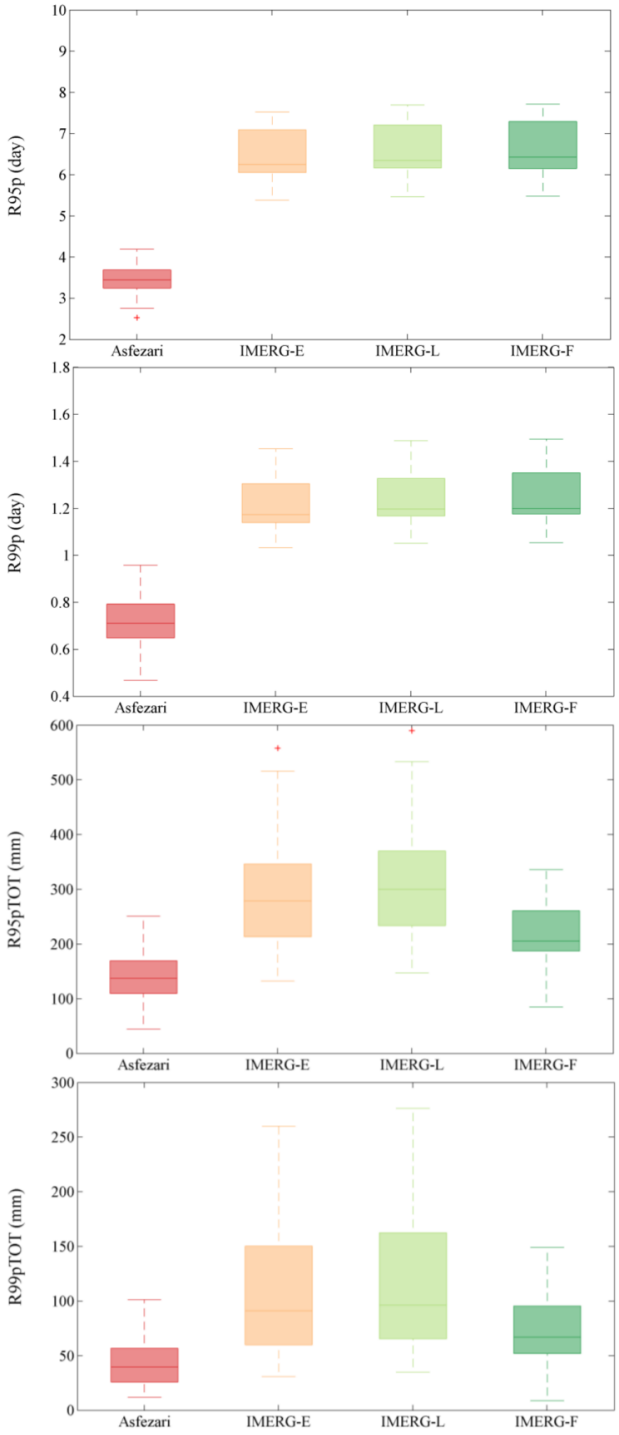

Figure 20. Relevant error box plots for Asfezari, IMERG-E, IMERG-L, and IMERG-F for grid-related threshold indices. The whiskers denote the maximum and minimum values in the data. The boxes extending from Q1 to Q3 show the median (red horizontal line) while the red + symbols show outliers.

 doi:10.20944/preprints202406.1173.v1

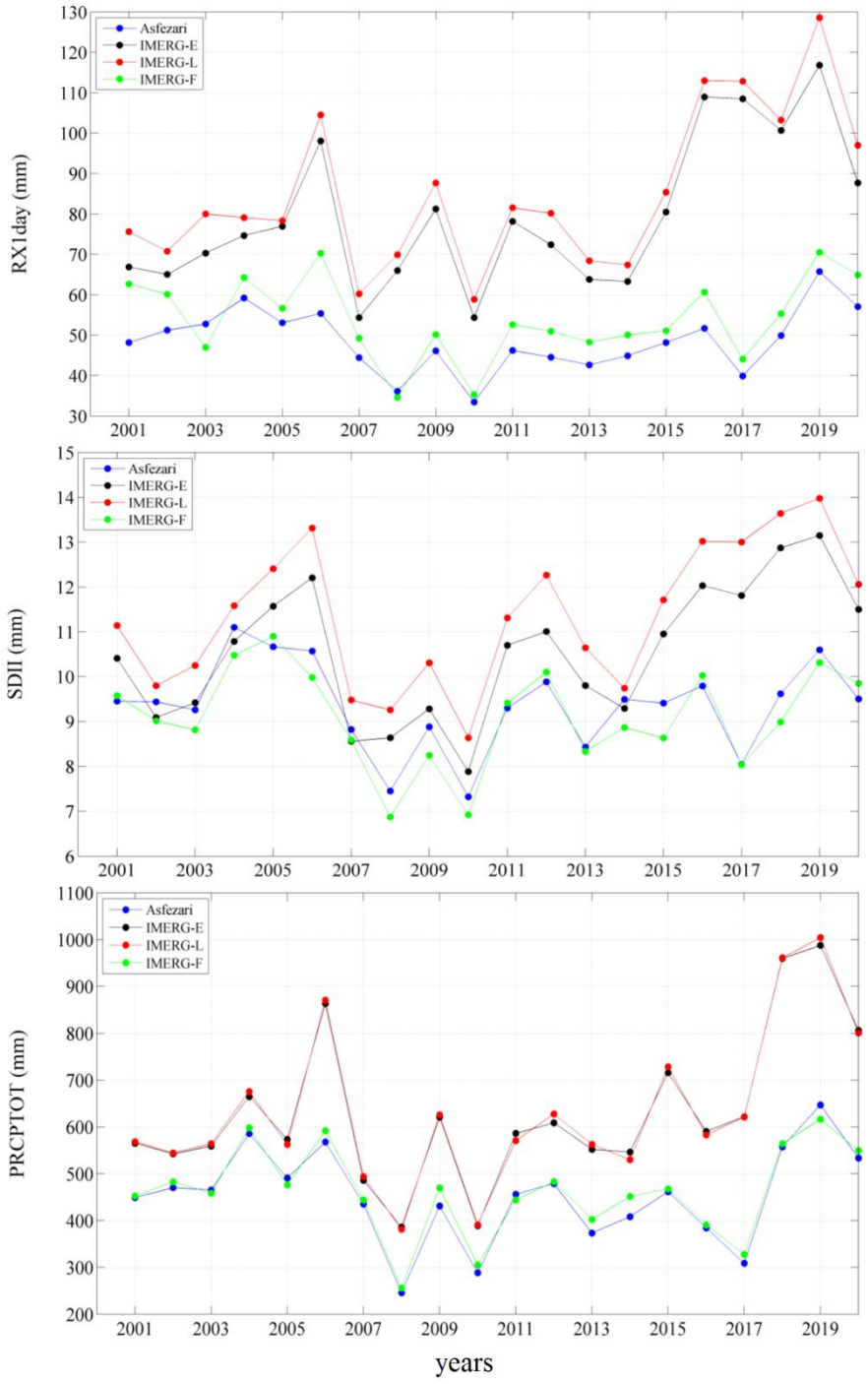

Figure 21. temporal variation of the non-threshold indices generated from Asfezari, IMERG-E, IMERG-L, and IMERG-F over 2001–2020.

 doi:10.20944/preprints202406.1173.v1

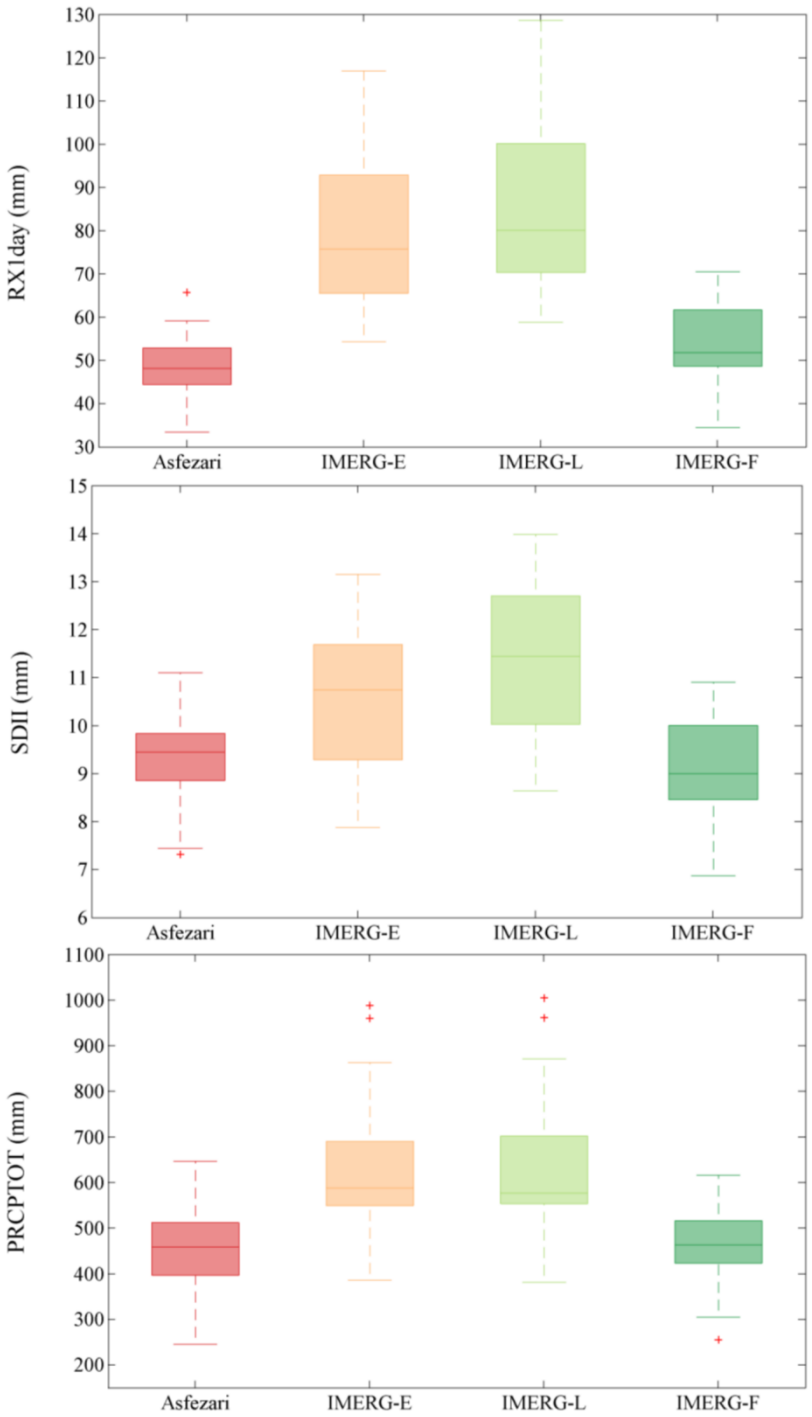

Figure 22. Relevant error box plots for Asfezari, IMERG-E, IMERG-L, and IMERG-F for non-threshold indices. The whiskers denote the maximum and minimum values in the data. The boxes extending from Q1 to Q3 show the median (red horizontal line) while the red + symbols show outliers.

10. Conclusion

The primary goal of this study was to comprehensively investigate IMERG-E, IMERG-L, and IMERG-F in precipitation estimation as well as their capability in detecting extreme rainfall events over southwestern Iran.

The findings suggest that:

(1) All three SPP's are generally successful in detecting precipitation events in the study area.

(2) All three SPP's are able to reproduce the basic inter-monthly precipitation climatology for the study area, but IMERG-E and IMERG-L overestimate rainfall totals in most months.

 doi:10.20944/preprints202406.1173.v1

(3) IMERG-F was superior in matching seasonal and annual rainfall amounts across the study area. IMERG-E and IMERG-L severely overestimated precipitation totals in the lowland areas north of the Persian Gulf. The overestimation appears to be related to the inland water bodies and permanent wetlands that cover the area of severe overestimation.

(4) Overall, IMERG-F was far superior in replicating spatial and temporal patterns in fixed threshold, grid-related threshold, and non-threshold extreme precipitation indices.

Overall, our results indicate that the IMERG-E and IMERG-L products, while available in near real time, must be used cautiously in detecting extreme precipitation events. IMERG-F data are far more accurate in the detection of extreme events, although not available in near real time. Consistent with our results, the skill of IMERG-F in detecting extreme precipitation indices has been reported in various previous studies [1,51,52]. Our study of southwestern Iran should add substantially to the understanding of how satellite-based products can be used in the detection of extreme precipitation events. Additionally, the results of the current study can possibly assist IMERG algorithm developers to improve the precipitation retrieval algorithms in both IMERG-E and IMERG-L over internal water bodies and permanent wetlands as well as elevated regions.

Author Contributions: Conceptualization, M.K.; methodology, M.K.; software, M.K.; validation, M.K., R.B.; formal analysis, X.X.; R.B; resources, M.K., R.B; data curation, M.K.; writing—original draft preparation, R.B; writing—review and editing, M.K., R.B.; visualization, M.K.; supervision, M.K., R.B; project administration, M.K.

Funding: This research received no external funding.

Data Availability Statement: Data will be available on request to the first author.

Acknowledgments: We are grateful to NASA for free access to the GPM IMERG data.

Conflicts of Interest: The authors declare no conflicts of interest.

References

1. Keikhosravi-Kiany, M.S., et al., Evaluation of Tropical Rainfall Measuring Mission, Integrated Multi-satellite Retrievals for GPM, Climate Hazards Centre InfraRed Precipitation with Station data, and European Centre for Medium-Range Weather Forecasts Reanalysis v5 data in estimating precipitation and capturing meteorological droughts over Iran. International Journal of Climatology, 2022. **42**(4): p. 2039-2064.
2. Dejene, I.N., M.B. Moisa, and D.O. Gemeda, Spatiotemporal monitoring of drought using satellite precipitation products: The case of Borena agro-pastoralists and pastoralists regions, South Ethiopia. Heliyon, 2023. **9**(3).
3. Pradhan, R.K., et al., Changes of precipitation regime and its indices over Rajasthan state of India: impact of climate change scenarios experiments. Climate Dynamics, 2019. **52**: p. 3405-3420.
4. Li, X., et al., Changes in precipitation extremes in the Yangtze River Basin during 1960–2019 and the association with global warming, ENSO, and local effects. Science of the Total Environment, 2021. **760**: p. 144244.
5. Arshad, M., et al., Evaluation of GPM-IMERG and TRMM-3B42 precipitation products over Pakistan. Atmospheric Research, 2021. **249**: p. 105341.
6. Shu, Z., et al., *Historical changes and future trends of extreme precipitation and high temperature in China.* Strategic Study of Chinese Academy of Engineering, 2022. **24**(5): p. 116-125.
7. Yang, J., et al., Changes of extreme precipitation in the middle and lower reaches of the Yangtze River and their correlation with atmospheric circulation. Frontiers in Earth Science, 2023. **11**: p. 1162220.
8. Trenberth, K.E., *Changes in precipitation with climate change.* Climate research, 2011. **47**(1-2): p. 123-138.
9. Aksu, H., et al., Spatial and temporal characterization of standard duration-maximum precipitation over Black Sea Region in Turkey. Natural Hazards, 2022: p. 1-27.
10. Kirschbaum, D., et al., Global distribution of extreme precipitation and high-impact landslides in 2010 relative to previous years. Journal of Hydrometeorology, 2012. **13**(5): p. 1536-1551.
11. Ávila, A., et al., *Recent precipitation trends, flash floods and landslides in southern Brazil.* Environmental Research Letters, 2016. **11**(11): p. 114029.
12. Marengo, J.A., et al., Extreme rainfall and hydro-geo-meteorological disaster risk in 1.5, 2.0, and 4.0 C global warming scenarios: an analysis for Brazil. Frontiers in Climate, 2021. **3**: p. 610433.
13. Trezzini, F., G. Giannella, and T. Guida, *Landslide and flood: economic and social impacts in Italy.* Landslide Science and Practice: Volume 7: Social and Economic Impact and Policies, 2013: p. 171-176.

 doi:10.20944/preprints202406.1173.v1

14. Winter, M.G., et al., *Economic impacts of landslides and floods on a road network.* AUC GEOGRAPHICA, 2019. **54**(2): p. 207-220.
15. Asadieh, B. and N.Y. Krakauer, *Global trends in extreme precipitation: climate models versus observations.* Hydrology and Earth System Sciences, 2015. **19**(2): p. 877-891.
16. Zittis, G., A. Bruggeman, and J. Lelieveld, *Revisiting future extreme precipitation trends in the Mediterranean.* Weather and Climate Extremes, 2021. **34**: p. 100380.
17. Sarachi, S., K.-l. Hsu, and S. Sorooshian, *A statistical model for the uncertainty analysis of satellite precipitation products.* Journal of Hydrometeorology, 2015. **16**(5): p. 2101-2117.
18. Battaglia, A., et al., Spaceborne cloud and precipitation radars: Status, challenges, and ways forward. Reviews of Geophysics, 2020. **58**(3): p. e2019RG000686.
19. Montazeri, M., M.S.K. Kiany, and S.A. Masoodian, Evaluation of Tropical Rainfall Measuring Mission (TRMM) Multi-satellite Precipitation Analysis (TMPA v7) in drought monitoring over southwest Iran. Climate Research, 2020. **82**: p. 55-73.
20. Houngnibo, M., et al., Validation of high-resolution satellite precipitation products over West Africa for rainfall monitoring and early warning. Frontiers in Climate, 2023. **5**: p. 1185754.
21. Keikhosravi-Kiany, M.S., S.A. Masoodian, and R.C. Balling Jr, *Reliability of satellite-based precipitation products in capturing extreme precipitation indices over Iran.* Advances in Space Research, 2023. **71**(3): p. 1451-1472.
22. Caloiero, T., G.N. Caroletti, and R. Coscarelli, *IMERG-based meteorological drought analysis over Italy.* Climate, 2021. **9**(4): p. 65.
23. Yu, L., G. Leng, and A. Python, A comprehensive validation for GPM IMERG precipitation products to detect extremes and drought over mainland China. Weather and Climate Extremes, 2022. **36**: p. 100458.
24. Weng, P., et al., Assessment of GPM IMERG and GSMaP daily precipitation products and their utility in droughts and floods monitoring across Xijiang River Basin. Atmospheric Research, 2023. **286**: p. 106673.
25. Wang, Z., et al., Evaluation of the GPM IMERG satellite-based precipitation products and the hydrological utility. Atmospheric Research, 2017. **196**: p. 151-163.
26. Nan, L., et al., Comprehensive evaluation of global precipitation measurement mission (GPM) IMERG precipitation products over Mainland China. Water, 2021. **13**(23): p. 3381.
27. Saouabe, T., et al., GPM-IMERG product: a new way to assess the climate change impact on water resources in a Moroccan semi-arid basin. Journal of Water and Climate Change, 2022. **13**(7): p. 2559-2576.
28. Fang, J., et al., Evaluation of the TRMM 3B42 and GPM IMERG products for extreme precipitation analysis over China. Atmospheric Research, 2019. **223**: p. 24-38.
29. Da Silva, N.A., et al., Validation of GPM IMERG extreme precipitation in the Maritime Continent by station and radar data. Earth and Space Science, 2021. **8**(7): p. e2021EA001738.
30. Ramadhan, R., et al., Capability of GPM IMERG products for extreme precipitation analysis over the Indonesian Maritime Continent. Remote Sensing, 2022. **14**(2): p. 412.
31. Zhang, D., et al., Can GPM IMERG capture extreme precipitation in North China Plain? Remote Sensing, 2022. **14**(4): p. 928.
32. Nepal, B., et al., Assessment of GPM-Era Satellite Products'(IMERG and GSMaP) ability to detect precipitation extremes over mountainous country Nepal. Atmosphere, 2021. **12**(2): p. 254.
33. Bakhtar, A., et al., Spatio-temporal evaluation of GPM-IMERGV6. 0 final run precipitation product in capturing extreme precipitation events across Iran. Water, 2022. **14**(10): p. 1650.
34. Kiany, M.S.K., et al., Evaluation of the TRMM 3B42 product for extreme precipitation analysis over southwestern Iran. Advances in Space Research, 2020.
35. Keikhosravi Kiany, M., et al., Spatial and Temporal Variations of Snow Cover in the Karoon River Basin, Iran, 2003–2015. Water, 2017. **9**(12): p. 965.
36. Raziei, T., et al., Spatial patterns and regimes of daily precipitation in Iran in relation to large-scale atmospheric circulation. International Journal of Climatology, 2012. **32**(8): p. 1226-1237.
37. Darand, M. and K. Khandu, Statistical evaluation of gridded precipitation datasets using rain gauge observations over Iran. Journal of Arid Environments, 2020. **178**: p. 104172.
38. Eini, M.R., et al., Evaluating three non-gauge-corrected satellite precipitation estimates by a regional gauge interpolated dataset over Iran. Journal of Hydrology: Regional Studies, 2021. **38**: p. 100942.
39. Shirgholami, M. and S.A. Masoodian, Analysis of Spatiotemporal Variations and Trends of Precipitation in Yazd Province by Asfezari Database During 1349 to 1394. Journal of Natural Environmental Hazards, 2023. **12**(35): p. 95-114.
40. Masoodian, S.A., *Asfezary National Gridded Daily Precipitation Data Base (Version 3).* Geography and Development, 2022. **20**(69): p. 107-127.
41. Tang, S., et al., Comparative evaluation of the GPM IMERG early, late, and final hourly precipitation products using the CMPA data over Sichuan Basin of China. Water, 2020. **12**(2): p. 554.
42. Su, J., et al., Evaluating the hydrological utility of latest IMERG products over the Upper Huaihe River Basin, China. Atmospheric Research, 2019. **225**: p. 17-29.

 doi:10.20944/preprints202406.1173.v1

43. Huffman, G.J., et al., NASA global precipitation measurement (GPM) integrated multi-satellite retrievals for GPM (IMERG). Algorithm Theoretical Basis Document (ATBD) Version, 2015. **4**: p. 26.
44. Sulla-Menashe, D. and M.A. Friedl, User guide to collection 6 MODIS land cover (MCD12Q1 and MCD12C1) product. USGS: Reston, VA, USA, 2018: p. 1-18.
45. Wang, H., et al., Extreme precipitation event over the Yellow Sea western coast: Is there a trend? Quaternary international, 2017. **441**: p. 1-17.
46. Wolff, D.B. and B.L. Fisher, Assessing the relative performance of microwave-based satellite rain-rate retrievals using TRMM ground validation data. Journal of applied meteorology and climatology, 2009. **48**(6): p. 1069-1099.
47. Peinó, E., J. Bech, and M. Udina, Performance assessment of GPM IMERG products at different time resolutions, climatic areas and topographic conditions in Catalonia. Remote Sensing, 2022. **14**(20): p. 5085.
48. Mahmoud, M.T., et al., Impact of topography and rainfall intensity on the accuracy of imerg precipitation estimates in an arid region. Remote Sensing, 2020. **13**(1): p. 13.
49. Navarro, A., et al., *Assessment of IMERG precipitation estimates over Europe.* Remote Sensing, 2019. **11**(21): p. 2470.
50. Huffman, G.J., et al., Integrated multi-satellite retrievals for the global precipitation measurement (GPM) mission (IMERG). Satellite precipitation measurement: Volume 1, 2020: p. 343-353.
51. Aksu, H., et al., Evaluation of IMERG for GPM satellite-based precipitation products for extreme precipitation indices over Turkiye. Atmospheric Research, 2023. **291**: p. 106826.